

Candidate List of Edge-on Galaxies with Substantial Extraplanar Dust

JONG-HO SHINN¹

¹*Korea Astronomy and Space Science Institute, 776 Daeduk-daero, Yuseong-gu, Daejeon, 305-348, the Republic of Korea*

Abstract

We present a list of edge-on galaxies that might have substantial extraplanar dust. Twenty-three edge-on galaxies were selected as target galaxies from an edge-on galaxy catalog, and their *Galaxy Evolution Explorer* far-ultraviolet images were fitted with three dimensional radiative transfer galaxy model. The galaxy model is described by two disks: one for the light source and the other for the dust. The best-fit parameters were found by employing a global optimization method, called differential evolution. To find the galaxies with substantial extraplanar dust using the best-fit parameters, we plotted the ratio of scale-height to galactic diameter: $z_s/D_{25,ph}$ (light source) vs $z_d/D_{25,ph}$ (dust). We found that 17 and 6 galaxies fall on the region of $(z_s/D_{25,ph} \times 100) > 0.2$ and $(z_s/D_{25,ph} \times 100) < 0.2$, respectively. The former is named as “high-group” and the latter is named as “low-group.” We conclude that “high-group” is likely to be the galaxies with substantial extraplanar dust, while “low-group” is likely to be the ones with little extraplanar dust, i.e. typical galactic thin disk, based on the following points: (1) the relative positions of “high-group” and “low-group” on the plot $z_s/D_{25,ph}$ vs $z_d/D_{25,ph}$ with respect to the reference values from optical radiative transfer studies; (2) the lower scale-height of the young stellar population than the old stellar population; and (3) a test result that shows the existence of extraplanar dust makes z_s and z_d overestimated in the fitting results. We also examined the dependence of the group separation on the surface density of far-ultraviolet luminosity ($L_{FUV}/D_{25,ph}^2$), but found no strong dependence.

Keywords: dust, extinction — galaxies: halos — galaxies: spiral — galaxies: structure — radiative transfer

1. INTRODUCTION

Galaxies evolve ever since their formation. Stars are forming, aging, and dying, while mediums are being expelled, accreted, and circulated. These mediums hold lots of information. They reveal the energy flow (e.g. galactic winds, [Veilleux et al. 2005](#)), and transform the spectral shape of intrinsic stellar lights (see [Hollenbach & Tielens 1999](#) and [Conroy 2013](#)). Also, they themselves are the raw materials for the future star formation. All these facts have close relations with the galactic energy distribution and hence the galaxy evolution. Dust is one constituent of the mediums, and it plays important roles in many ways despite its mere $\sim 0.1\%$ occupation of the baryonic mass ([Blanton & Moustakas 2009](#)).

The extraplanar dust, located above the galactic plane, is of importance in diverse aspects as noted in [Shinn & Seon \(2015\)](#). It manifests that some mechanism makes the dust to be located away from the galactic plane defying the gravity. It might also hold some hints on the connection between star-forming and star-bursting galaxies (see [Kennicutt & Evans 2012](#)) and between interstellar and intergalactic mediums (see [Meiksin 2009](#); [Putman et al. 2012](#)), since dust can move between the galactic plane and halo through the accretion and ejection processes. Additionally, the extraplanar dust is worthy of meticulous study in the sense that the dust-scattered $H\alpha$ could substantially contaminate the extraplanar $H\alpha$ features ([Seon & Witt 2012](#)) which is attributed to the diffuse ionized gas (see [Haffner et al. 2009](#)). Many studies on the extraplanar dust, therefore, had been carried out at diverse wavelengths (e.g. [Howk & Savage 1997, 1999](#); [Howk 1999](#); [Thompson et al. 2004](#); [Popescu et al. 2004](#); [Irwin & Madden 2006](#); [Irwin et al. 2007](#); [Seon et al. 2014](#); [Hodges-Kluck & Bregman 2014](#); [Shinn & Seon 2015](#); [Hodges-Kluck et al. 2016](#)).

To better understand how the extraplanar dust works in the context of galaxy evolution, three-dimensional physical modeling of the galaxy is useful as much as phenomenological analyses of observable quantities, given that one can extract more fundamental galactic parameters such as scale-height. [Seon et al. \(2014\)](#) had first attempted this approach focusing on the extraplanar dust, and successfully modeled the dust-scattered ultraviolet halo of an edge-on galaxy, NGC 891. They used a galaxy model including a geometrically-thick dust disk in addition to the thin disk, and obtained several galactic parameters such as star formation rate, dust scale-height, face-on dust optical depth, light source scale-height, etc. In order to determine whether there is any relation between the properties of extraplanar dust and host galaxy, [Shinn & Seon \(2015\)](#) extended the approach of [Seon et al. \(2014\)](#) to six highly-inclined galaxies that were reported to have ultraviolet halos ([Hodges-Kluck & Bregman 2014](#)). However, [Shinn & Seon \(2015\)](#) found that the additional geometrically-thick dust disk might not be required for three out of those six galaxies to reproduce the observed ultraviolet halos.

This finding suggests that the visual identification of galactic ultraviolet halos, without the aid of three-dimensional physical modeling, is less reliable in judging the existence of substantial extraplanar dust. Obviously, a reliable target list is crucial for the investigation of the extraplanar dust. Here we present a list of edge-on galaxies that seem to have substantial extraplanar dust, as a preparation for the future study on their extraplanar dust. The list was produced from the edge-on disk galaxy catalog of [Bizyaev et al. \(2014\)](#) by performing model fittings to ultraviolet images from *Galaxy Evolution Explorer* (*GALEX*). We found that 17 out of 23 target galaxies seem to have substantial extraplanar dust.

2. DATA AND TARGET SELECTION

GALEX ultraviolet images were used for our study on the galactic extraplanar dust as in [Shinn & Seon \(2015\)](#). Ultraviolet wavelength has an advantage in exposing the extraplanar dust through scattering processes, since the dominant ultraviolet light sources—massive stars—reside in the galactic plane with a *smaller* scale-height than the old stellar population ([Bahcall & Soneira 1980](#); [Wainscoat et al. 1992](#); [Martig et al. 2014](#)). Indeed, several studies using ultraviolet data have claimed the detection of dust-scattered ultraviolet halos around edge-on galaxies ([Seon et al. 2014](#); [Hodges-Kluck & Bregman 2014](#); [Shinn & Seon 2015](#); [Hodges-Kluck et al. 2016](#)). Besides, one of the studies provided the galactic parameters that excellently reproduce a panchromatic galactic spectral energy distribution ([Baes & Viaene 2016](#)).

GALEX provides wide-field ($\sim 1.25^\circ$) images at two ultraviolet bands (FUV: 1344 – 1786 Å; NUV: 1771 – 2831 Å) with imaging resolutions of $\sim 4'' - 5''$ ([Morrissey et al. 2007](#)). It covered almost all sky at both bands except the Galactic plane ([Bianchi et al. 2014](#)), hence *GALEX* data are well-suited for statistical studies of a large sample. We used the archival data of GR6/7 (<http://galex.stsci.edu/GR6/>) and no additional data reduction procedure was applied except cropping and masking. The standard pipeline procedures are described in [Morrissey et al. \(2007\)](#). Only the FUV images were analyzed for several reasons as mentioned in [Shinn & Seon \(2015\)](#): narrower bandwidth, smoother albedo variation over the bandwidth, and fewer foreground point sources.

We chose our target galaxies from the edge-on galaxy catalog of [Bizyaev et al. \(2014\)](#). The catalog is based on the optical images from the Seventh Data Release (DR7; [Abazajian et al. 2009](#)) of *Sloan Digital Sky Survey* (*SDSS*; [York et al. 2000](#)), and the genuine edge-on galaxies were selected through both automatic and visual inspections. The catalog lists 5794 edge-on galaxies as of November 2014, along with their structural parameters for stellar disks derived from 1D (ignoring dust extinction) and 3D (including dust absorption only) analyses, respectively.

We first narrowed down the catalog to 119 target galaxies by applying the following constraints one after another. To select galaxies with large enough angular sizes, the scale-length from the 1D analysis is limited to be $\geq 10''$ in any of three bands (g , r , i). We then secured high signal-to-noise ratios (S/Ns) by limiting the *GALEX* FUV exposure time to be ≥ 1000 s. The distance to the galaxies are essential for our analysis, therefore we excluded the galaxies if their distance information is not available from the NASA/IPAC Extragalactic Database (<https://ned.ipac.caltech.edu/>). Finally, we excluded those galaxies that show ring features in their *GALEX* FUV images or fall on the edge of the *GALEX* field-of-view.

In this study, the existence of extraplanar dust is revealed by the galactic off-plane lights which are much weaker than the galactic in-plane lights. This means that the higher S/N data give us the more reliable information about the extraplanar dust. In this sense, we winnowed once again the 119 targets to the final 23 targets that show S/N per pixel ≥ 3 continuously along the galactic disk. The S/N was solely calculated from the photon count itself. We checked if any artifacts from the instrumental scattered light mentioned in [Hodges-Kluck & Bregman \(2014\)](#) affect our

target galaxy images, and found none. It seems to be due to the lower sensitivity of the *GALEX* FUV band than the NUV (Morrissey et al. 2007) and the rarity of the stars bright in the FUV band. Fig. 1 shows the *GALEX* FUV and *SDSS* images of 23 target galaxies, and Table 1 lists the relevant target information.

3. ANALYSIS AND RESULTS

The purpose of this study is to search for the galaxies that are likely to have substantial extraplanar dust. To find these galaxies, we fitted the *GALEX* images of the target galaxies (Fig. 1 and Table 1) with a three dimensional radiative transfer galaxy model whose dust component is described by a *single* disk. Under this scheme, the galaxies with *little* extraplanar dust would return typical scale-heights of light-source and dust. On the other hand, those galaxies with *substantial* extraplanar dust would return distinct scale-heights or systematic (not random) fitting residuals, or both, because the extraplanar dust would affect the radiative transfer of the stellar light. This point is more elaborated in section 3.2 while mentioning Test C. In the following, we describe the radiative transfer galaxy model and fitting procedure (section 3.1); test fitting results (section 3.2); and target fitting results (section 3.3).

3.1. Radiative Transfer Galaxy Model and Fitting Procedure

We adopted a galaxy description for the fitting as below, which is equal to the one used in Shinn & Seon (2015) except the additional thick dust disk we excluded here.

$$\kappa(r, z) = \begin{cases} \kappa_0 \exp\left(-\frac{r}{h_d} - \frac{|z|}{z_d}\right), & \text{for } r \leq R_d \\ 0, & \text{for } r > R_d \end{cases} \quad (1)$$

$$I(r, z) = \begin{cases} I_0 \exp\left(-\frac{r}{h_s} - \frac{|z|}{z_s}\right), & \text{for } r \leq R_s \\ 0, & \text{for } r > R_s \end{cases} \quad (2)$$

Here, $\kappa(r, z)$ and $I(r, z)$ are the distributions of extinction coefficient and light source, respectively. h_d , h_s , z_d , and z_s are the corresponding radial scale-length and vertical scale-height of dust and light source. κ_0 is the extinction coefficient at the center of the galaxy ($r = 0$, $z = 0$), where the optical depth along the symmetric axis (τ_{FUV}) is $2 \kappa_0 z_d$. I_0 is the light-source density at the center of the galaxy ($r = 0$, $z = 0$). The four parameters (I_0 , h_s , z_s , and R_s) determine the galactic luminosity (L_{FUV}). R_d and R_s are the truncation radii of dust and light source, respectively. The radiative transfer calculations were performed at the wavelength of 1538.6 Å, i.e. the effective wavelength of *GALEX* FUV band (Morrissey et al. 2007) using the three dimensional Monte-Carlo method (see Steinacker et al. 2013). Basically, the model produces a two dimensional synthetic image toward the observer, by calculating how many photons arrive at the observer after traveling the three dimensional model galaxy described by eqs. (1) and (2), while being scattered and absorbed by dust. Readers are referred to Seon et al. (2014) and Shinn & Seon (2015) for more details on the radiative transfer calculations.

In contrast to our previous work (Shinn & Seon 2015), we neither rotated the *GALEX* image to align the major axis of the target galaxy to horizontal direction, nor subtracted the background from the *GALEX* image before the fitting. We instead enabled the galaxy model to rotate during the fitting process and treated the background as free parameters. The background was also set to have linear gradients along the horizontal and vertical directions of the *GALEX* image. The model galaxy was free to move in both directions during the fitting. In summary, six parameters were newly added: the position angle of the galaxy (θ_{pos}), horizontal and vertical shifts of the galaxy center at the image plane (Δx , Δy), the background level at the center of the image (bg_{ctr}), and the horizontal and vertical gradients of the background at the center of the image ($\partial bg/\partial x$, $\partial bg/\partial y$). Now we have 15 free parameters to fit—eight parameters are for the model galaxy itself (L_{FUV} , τ_{FUV} , h_d , z_d , R_d , h_s , z_s , R_s) and the other seven parameters are for the viewpoint and the background (θ_{incl} , θ_{pos} , Δx , Δy , bg_{ctr} , $\partial bg/\partial x$, $\partial bg/\partial y$); θ_{incl} is the inclination angle of model galaxy.

When generating the model image, the spatial convolution procedure was included at the last stage to match the spatial resolutions of the model image and the *GALEX* image. We used a new custom point-spread-function (PSF). This PSF is based on the *GALEX* PSF, but extended up to the PSF image size of 600'' in the same way as Shinn & Seon (2015) did: the part where the radial distance $\gtrsim 50''$ was extrapolated from a functional fit. We adopted this extended PSF to include the instrumental effects that might vertically broaden the galactic plane emission (see Sandin 2014, 2015). The convolution was carried out through the Fourier transformation for speed.

We prepared the images for the fitting as follows. The fitting area was manually set not to be overwhelmed by the background area, since, if not, the goodness of fit would be primarily determined by the background area. Bright point sources and uninterested extended features were also masked. The white areas around the galaxy images (Fig. 2-27) indicate the excluded regions during the model fitting.

We found the best-fit model by maximizing the likelihood $\mathcal{L}(M|D)$, where M and D stand for the 15 model parameters and the *GALEX* FUV image, respectively. Poisson distribution was adopted as the parent probability distribution for each image pixel, because the photon counts per pixel of *GALEX* image is too small to be treated as Gaussian (see the *GALEX* count image in Fig. 5-27). Therefore, the likelihood was calculated from the images in *count* units (not *count per sec*): the *GALEX* FUV *count* image and the model image which is converted into *count* units using the *GALEX* relative response image (see Morrissey et al. 2007). In this case, maximizing the likelihood corresponds to minimizing the C -statistic (Cash 1979), not the χ^2 -statistic: $C = -2 \sum_i (d_i \ln m_i - m_i - \ln d_i!)$, where m_i and d_i are the pixel values of the model and data images, respectively.

Since it is highly uncertain if the likelihood has local maxima or not, partly due to the complex nature of radiative transfer and the large number of free parameters, we employed a global optimization method called Differential Evolution (DE; Storn & Price 1997). This technique finds the global maximum by making numerous parameter vectors search the likelihood surface through iterations as follows. Suppose we have D number of model parameters, and they consist of the parameter vector $\mathbf{x} = (p_1, p_2, \dots, p_D)$. (1) NP number of parameter vectors are generated over some reasonable parameter ranges: each parameter of a vector \mathbf{x} is *randomly-and-independently* generated. That is, we have the vector population $[\mathbf{x}_1, \mathbf{x}_2, \dots, \mathbf{x}_{NP}]$. This population is called the 1st generation, say $\mathbb{X}^{(1)} = [\mathbf{x}_1^{(1)}, \mathbf{x}_2^{(1)}, \dots, \mathbf{x}_{NP}^{(1)}]$. (2) Among the vector population, one vector is set as the target vector. (3) Three vectors are *randomly* chosen from the rest of the parameter vectors. These three are mutated *parameter-wise* to be the mutant vector: that is, $\mathbf{x}_{\text{mt}} = \mathbf{x}_{\text{1st}} + F \times (\mathbf{x}_{\text{2nd}} - \mathbf{x}_{\text{3rd}})$ where F is an arbitrary constant. (4) The mutant vector becomes the trial vector through the ‘‘crossover’’ process, where some of the parameters being replaced with the target vector’s. Whether the parameter is replaced or not is determined by a random number which ranges from 0 to 1. When the random number for each parameter is greater than CR , an arbitrary constant, the corresponding parameter is replaced with the target vector’s. (5) The two likelihoods are respectively calculated with the target vector and the trial vector, and then compared each other. If the trial vector’s likelihood is greater than that of the target vector, the target vector is replaced with the trial vector in the next generation; if not, the target vector remains in the next generation. (6) A new target vector is set. It is chosen from the vectors in the current generation that has not been the target vector before. (7) The processes (3)-(6) are repeated until all vectors have been the target vector. (8) Then, we have the 2nd generation of the vector population $\mathbb{X}^{(2)}$. (9) With the 2nd generation, repeat the processes (2)-(7), and then we have the 3rd generation $\mathbb{X}^{(3)}$, and so on. (10) When each parameter of the vector population converges to a certain range, then the best-fit vector is selected among the population as the one that shows the highest likelihood value.

During the fitting, we impose some constraints as follows. In the sequence (1), we randomly sampled the scale-length and scale-height parameters so that they are uniformly distributed in log scale, while sampling the other parameters to be uniform in linear scale. In the sequence (4), we put the parameters back to the initial parameter range limits, when the trial vector exceeds the limits. Also, we set a constraint of $R_s \leq R_d$, in order to avoid the case that the light source is situated on dust-free space, which seems unlikely for massive stars (the dominant UV sources).

We show the results of DE fitting in the next two sub-sections. In section 3.2, we produce mock observation images and demonstrate how well the DE fitting method reproduces the model input values that are used for making the mock images. The fitting results for the *GALEX* images follow in section 3.3.

3.2. Test: Fitting the Mock Observation Images

We employed the DE method to find the best-fit parameters of the galaxy model. The DE method has three control variables (NP, F, CR) that should be adjusted by trial and error. NP is the number of parameter vectors, F is a factor that scales the parameter difference when the mutant vector is created, and CR is the crossover constant which determines how many parameters of the mutant vector will be replaced with the ones of the target vector when the trial vector is created (Storn & Price 1997); these three variables are related with the sequences (1), (3), and (4) mentioned in section 3.1, respectively. To determine these variables and see if the DE method works properly for our study, we ran several test fittings to the mock observation images and checked how much the obtained parameters are close to the model input values. The mock images were produced from the model described in eqs. (1) and (2) with 5×10^8 photons, and the background emission was set to zero for simplicity. The same three dimensional model-grid

was used for both producing and fitting the mock observation images. The number of grid cells were (radial, azimuthal, vertical)=(30, 1, 61) in cylindrical coordinates, and the cell size was set to scale exponentially from the galaxy center to cover a larger space as being further away from the center.

Three different tests were carried out and the results are shown in Fig. 2-4. We adopted $NP = 90$, $F = 0.5$, and $CR = 0.9$, and obtained a converged population within 500 iterations. Iterations of 250 took about 1.5 – 2.0 hrs with 88 CPUs; the CPU model is the Intel(R) Xeon(R) CPU E5-2699 v4 @ 2.20GHz. During the fitting, each model image was produced with 5×10^6 photons, much less than used for producing the mock image, for speed.

Fig. 2 displays the results of Test A. Test A represents an edge-on galaxy that shows an absorption feature along the galactic plane. To show the goodness of fit more intuitively, we show the χ^2 image rather than the C -statistic image. The uncertainty of each pixel was set as $1 + \sqrt{\text{count} + 0.75}$, the $1\text{-}\sigma$ upper limit for small number events (Gehrels 1986), rather than the conventional $\sqrt{\text{count}}$ in order to reflect the small counts of *GALEX* image. As the results show, the DE method well reproduces the model input values. R_d is the least converging parameter as its relatively broader population distribution shows at the end of the iteration.

Fig. 3 shows the results of Test B, which represents an edge-on galaxy *without* an absorption feature along the galactic plane. In this test, again, the DE method well reproduce the model input values, although the inclination angle had been confused at the beginning of the iteration. The confusion might be related with the absence of the absorption feature at the galactic plane, which hints the direction of galaxy inclination. R_d is again the least converging parameter.

Fig. 4 displays the results of Test C. We performed this test in order to see how the fitting results might look like when the target has substantial extraplanar dust. To simulate the existence of substantial extraplanar dust, we added a second dust disk as adopted in Seon et al. (2014) and Shinn & Seon (2015). Note that a spherical dust halo was adopted for the extraplanar dust in Hodges-Kluck & Bregman (2014). In summary, Test C demonstrates how the best-fit parameters turn out when *two dust disks (thin and thick)* exists but the data is fitted with the conventional *one-component dust disk* like our approach in this work.

The χ^2 image of Fig. 4 shows that there is a systematic variation of χ^2 along the galactic plane with higher χ^2 values than those of Test A and Test B. Note that z_d converges to the value between the two input values (dust scale-heights for thin and thick disks) and that z_s converges to the value higher than the input value (light-source scale-height). This means that the galaxies with substantial extraplanar dust would return higher z_d and z_s values than the typical ones. Test C results also show that other parameters such as R_d , θ_{incl} , and Δy might also be affected by the existence of substantial extraplanar dust.

3.3. Fitting the *GALEX* Images

Keeping the results of Test C (section 3.2) in mind, we performed the model fitting to the *GALEX* FUV images of the 23 target galaxies (Fig. 1 and Table 1) in order to select the candidate galaxies with substantial extraplanar dust. The control variables of DE method were adopted as $NP = 113$, $F = 0.5$, and $CR = 0.9$. Only NP was changed from the test ones, from 90 to 113, to properly handle the increased number of fitting parameters; the three background parameters (bg_{ctr} , $\partial bg/\partial x$, and $\partial bg/\partial y$) were additionally set as free parameters. The configuration of three dimensional model grid was the same with the test one (section 3.2), and its physical size was set as that of the *GALEX* image's diagonal (say, tens of kpc).

We ran the fitting three times with different 1st generation parameter vectors, and found three best-fit parameter sets. Figures 5-27 show one set of the results. On average, the iteration of 250 took about 2 – 3 hrs, a little longer than the test cases (section 3.2); when the photon has to travel through a denser dust medium (e.g. higher τ_{FUV} , h_d , and z_d), the run time was doubled or more. For most of the target galaxies, the fitting parameters were converged within 500 iterations, but some targets needed > 1000 iterations to converge. The χ^2 images were made in the same way with the test cases (Fig. 2-4), and the region of $\chi^2 < 3$ is dominant in most of the targets. However, some targets (e.g. EON_24.788.-10.504, EON_163.623.17.344) show several regions with high residuals, which seems to be due to bright (or dark) local features. Table 2 shows the best model parameters with errors. The mean and standard deviation of the three best-fit parameter sets are quoted as the best model parameters and their errors, respectively, in a similar way to De Geyter et al. (2013) and De Geyter et al. (2014).

Fig. 28 shows how light sources and dust distribute in terms of scale-heights and scale-lengths. It shows that z_s is smaller than z_d for all targets except EON_20.349.-1.863 and EON_189.100.40.005, while h_s and h_d are almost

randomly distributed on either sides of the one-to-one line. Large h_s and h_d (> 100 kpc) mean the relatively uniform distribution of light source and dust along the radial direction.

To find the candidate galaxies with substantial extraplanar dust, we plot the $z_s/D_{25,ph}$ vs $z_d/D_{25,ph}$ (Fig. 29a). If the galactic disk is the manifestation of the equilibrium between internal kinetic pressure and gravitational force (see Spitzer 1942), the scale-height would be proportional to the galactic mass (and roughly to the galactic diameter). Therefore, the spiral galaxies in dynamical equilibrium would fall into a certain region in the plot of $z_s/D_{25,ph}$ vs $z_d/D_{25,ph}$. Under these circumstances, we expect that the galaxies with substantial extraplanar dust would fall on a distinct region from the stable spiral galaxies, as Test C (section 3.2) shows that the existence of substantial extraplanar dust make z_s and z_d overestimated.

Our fitting results are plotted as circles in Fig. 29a, and the circles show two distinct distributions. One group is on the region $(z_s/D_{25,ph} \times 100) > 0.2$ (*open circles*), while the other is on the region $(z_s/D_{25,ph} \times 100) < 0.2$ (*filled circles*). We name the former and the latter as “high-group” and “low-group,” respectively. “high-group” contains 17 galaxies, while “low-group” contains 6 galaxies. To help the identification of these two groups, we plot together the values of other edge-on galaxies (*gray squares*) obtained from optical radiative transfer studies (Table 4). These *gray squares* represent the galactic thin disks (see Freeman & Bland-Hawthorn 2002), and occupy the lower-right corner of Fig. 29a.

In Fig. 29b, we compare the $L_{FUV}/D_{25,ph}^2$ and $z_d/D_{25,ph}$ to see if the FUV luminosity plays any role in separating “high-group” and “low-group,” since the luminosity is one important physical parameter of the host galaxy. The factor $D_{25,ph}^2$, proportional to the galactic disk area, is used for scaling the luminosity to compensate the size difference among galaxies. As Fig. 29b shows, no prominent difference of $L_{FUV}/D_{25,ph}^2$ exists between “high-group” and “low-group,” although “high-group” seems to have somewhat lower values. This means that $L_{FUV}/D_{25,ph}^2$ is not sensitive in separating “high-group” and “low-group.”

4. DISCUSSION

As seen in Fig. 29a, “high-group” and “low-group” occupy the right and left regions, respectively. The reference values for comparison (*gray squares*) are located at the lower-right corner. These reference values are from optical radiative transfer studies (Table 4), and represent the galactic thin disk (see Freeman & Bland-Hawthorn 2002); hence, they would help to identify “high-group” and “low-group.” As in the following two paragraphs, we conclude that “high-group” likely represents the galaxies with *substantial* extraplanar dust, while “low-group” likely represents the ones with *little* extraplanar dust.

“Low-group” shows lower $z_s/D_{25,ph}$ than the reference values, while showing similar $z_d/D_{25,ph}$ to the reference values. Considering that the reference values are from optical studies, the reference z_s values represent the old stellar population. On the other hand, our z_s represent the young stellar population, since our z_s are from ultraviolet data analyses. As mentioned in section 2, the young stellar population has a *smaller* scale-height than the old stellar population (Bahcall & Soneira 1980; Wainscoat et al. 1992; Martig et al. 2014). Therefore, smaller $z_s/D_{25,ph}$ of “low-group” than the reference values can be understood on the basis of stellar population difference. Based on this explanation on $z_s/D_{25,ph}$, as well as the similarity of $z_d/D_{25,ph}$ between “low-group” and the reference values, we think that “low-group” likely represents the galactic thin disks, i.e. galaxies with little extraplanar dust.

“High-group” shows similar $z_s/D_{25,ph}$ to the reference values, while showing similar or higher $z_d/D_{25,ph}$ than the reference values. The z_s of “high-group” comparable to the reference values is contradictory to the fact that the young stellar population has a lower scale-height than the old stellar population. It is hard to imagine any dynamical process that can spread the young stellar population more away from the galactic plane as a factor of ~ 10 than the typical thin disk (“low-group”). The higher $z_d/D_{25,ph}$ than the reference values which some “high-group” galaxies show might simply be interpreted as the existence of substantial dust above the galactic plane. In section 3.2, Test C shows that the existence of substantial extraplanar dust make z_s and z_d overestimated in the fitting results. Considering these test results as well as the contradictory $z_s/D_{25,ph}$ and the higher $z_d/D_{25,ph}$, we think that “high-group” is likely to be the galaxies with substantial extraplanar dust. In other words, “high-group” is hard to be explained within the framework of galactic thin disk.

We additionally note that one target from the optical radiative transfer studies, NGC 4302, happens to be on our target list as EON_185.427_14.598. This target belongs to “high-group,” and its optical study showed poor fitting results that remains big residual features at the bulge and halo regions (Bianchi 2007). These large residuals might

be caused by the substantial extraplanar dust in NGC 4302, rather than the additional stellar disk as suspected by Bianchi (2007).

In Fig. 29b, “high-group” and “low-group” show no stark difference along the axis of $L_{FUV}/D_{25,ph}^2$. This means that $L_{FUV}/D_{25,ph}^2$ is not a good discriminator for the galaxies with substantial extraplanar dust. Test C in section 3.2 shows a consistent result that the best-fit L_{FUV} is not much different from the input value for the mock data even when substantial extraplanar dust exists. For “low-group” which likely represents the galactic thin disk, we could examine any relation between $z_d/D_{25,ph}$ and $L_{FUV}/D_{25,ph}^2$. However, the number of members in “low-group” (six) is too small to remark on any relation. The same kind examination is improper for “high-group.” The fitting parameters of “high-group” were obtained from an *improper* model (single dust disk) which does not include a description for the extraplanar dust. Any relation between the properties of the extraplanar dust and the host galaxy must be studied with the model that includes a proper description for the extraplanar dust, such as a geometrically-thick dust disk assumed in Shinn & Seon (2015) or a spherical dust halo assumed in Hodges-Kluck & Bregman (2014). Model selection (see Sharma 2017) would be required to determine which model is better at describing the extraplanar dust. Then, based on the better model, we can obtain the model parameters that characterize the extraplanar dust through the parameter estimation process.

5. CONCLUSIONS

To list the candidate galaxies with substantial extraplanar dust, we fitted the *GALEX* FUV images of edge-on galaxies using three dimensional radiative transfer model. The DE method was employed to find a global maximum in the highly complex likelihood surface. Twenty-three galaxies were selected as target galaxies from the edge-on galaxy catalog of Bizyaev et al. (2014). The best model parameters were analyzed by plotting the ratios of scale-height to galactic diameter (Fig. 29a): $z_s/D_{25,ph}$ for light source and $z_d/D_{25,ph}$ for dust. We found that 17 galaxies are populated at the region of $(z_s/D_{25,ph} \times 100) > 0.2$ (“high-group”), while the rest six (“low-group”) are populated at the region of $(z_s/D_{25,ph} \times 100) < 0.2$. To help the identification of these two groups, we plotted the corresponding values of other galaxies from optical radiative transfer studies (Table 4). These optical reference values represent the galactic thin disks and are populated at the lower-right corner of the plot $z_s/D_{25,ph}$ vs $z_d/D_{25,ph}$ (Fig. 29a).

We conclude that “low-group” likely represents the galactic thin disk (i.e. galaxies with little extraplanar dust), while “high-group” likely represents the ones with substantial extraplanar dust, based on the followings: (1) the positions of “low-group” and “high-group” relative to the optical reference values in the plot of $z_s/D_{25,ph}$ versus $z_d/D_{25,ph}$ (Fig. 29a); (2) $z_s/D_{25,ph}$ from ultraviolet data analysis should be lower than $z_s/D_{25,ph}$ from optical data analysis, because the optical light sources are the old stellar population while the ultraviolet light sources are the young stellar population; and (3) Test C in section 3.2 shows that the existence of substantial extraplanar dust makes z_s and z_d overestimated in the fitting results. The distributions of “low-group” and “high-group” along the luminosity values ($L_{FUV}/D_{25,ph}^2$) were also examined. We found that the group separation does not sensitively depend on $L_{FUV}/D_{25,ph}^2$ values, which is also observed in the result of Test C (section 3.2).

The candidate galaxies with substantial extraplanar dust we found (“high-group”) would be useful for studying the relation between the properties of the extraplanar dust and the host galaxy. Prior to this study, a proper model well describing the extraplanar dust must be determined through model selection.

J.-H.S. appreciate the anonymous referee’s comments that improve the manuscript substantially. J.-H.S. is also grateful to Kwang-Il Seon for providing the galaxy model, to Yujin Yang for his helpful comments on the manuscript, and to Young-Dae Lee for his help in retrieving *GALEX* data with a script.

REFERENCES

- | | |
|---|--|
| <p>Abazajian, K. N., Adelman-McCarthy, J. K., Agüeros, M. A., et al. 2009, <i>ApJS</i>, 182, 543,
doi: 10.1088/0067-0049/182/2/543</p> <p>Baes, M., & Viaene, S. 2016, <i>A&A</i>, 587, A86,
doi: 10.1051/0004-6361/201527812</p> | <p>Bahcall, J. N., & Soneira, R. M. 1980, <i>ApJS</i>, 44, 73,
doi: 10.1086/190685</p> <p>Bianchi, L., Conti, A., & Shiao, B. 2014, <i>AdSpR</i>, 53, 900,
doi: 10.1016/j.asr.2013.07.045</p> <p>Bianchi, S. 2007, <i>A&A</i>, 471, 765,
doi: 10.1051/0004-6361:20077649</p> |
|---|--|

- Bizyaev, D. V., Kautsch, S. J., Mosenkov, A. V., et al. 2014, *ApJ*, 787, 24, doi: [10.1088/0004-637X/787/1/24](https://doi.org/10.1088/0004-637X/787/1/24)
- Blanton, M. R., & Moustakas, J. 2009, *ARA&A*, 47, 159, doi: [10.1146/annurev-astro-082708-101734](https://doi.org/10.1146/annurev-astro-082708-101734)
- Cash, W. 1979, *ApJ*, 228, 939, doi: [10.1086/156922](https://doi.org/10.1086/156922)
- Conroy, C. 2013, *ARA&A*, 51, 393, doi: [10.1146/annurev-astro-082812-141017](https://doi.org/10.1146/annurev-astro-082812-141017)
- De Geyter, G., Baes, M., Camps, P., et al. 2014, *MNRAS*, 441, 869, doi: [10.1093/mnras/stu612](https://doi.org/10.1093/mnras/stu612)
- De Geyter, G., Baes, M., Fritz, J., & Camps, P. 2013, *A&A*, 550, A74, doi: [10.1051/0004-6361/201220126](https://doi.org/10.1051/0004-6361/201220126)
- de Looze, I., Baes, M., Bendo, G. J., et al. 2012, *MNRAS*, 427, 2797, doi: [10.1111/j.1365-2966.2012.22045.x](https://doi.org/10.1111/j.1365-2966.2012.22045.x)
- Freeman, K., & Bland-Hawthorn, J. 2002, *ARA&A*, 40, 487, doi: [10.1146/annurev.astro.40.060401.093840](https://doi.org/10.1146/annurev.astro.40.060401.093840)
- Gehrels, N. 1986, *ApJ*, 303, 336, doi: [10.1086/164079](https://doi.org/10.1086/164079)
- Haffner, L. M., Dettmar, R.-J., Beckman, J. E., et al. 2009, *RvMP*, 81, 969, doi: [10.1103/RevModPhys.81.969](https://doi.org/10.1103/RevModPhys.81.969)
- Hodges-Kluck, E., & Bregman, J. N. 2014, *ApJ*, 789, 131, doi: [10.1088/0004-637X/789/2/131](https://doi.org/10.1088/0004-637X/789/2/131)
- Hodges-Kluck, E., Cafmeyer, J., & Bregman, J. N. 2016, *ApJ*, 833, 58, doi: [10.3847/1538-4357/833/1/58](https://doi.org/10.3847/1538-4357/833/1/58)
- Hollenbach, D. J., & Tielens, A. G. G. M. 1999, *RvMP*, 71, 173, doi: [10.1103/RevModPhys.71.173](https://doi.org/10.1103/RevModPhys.71.173)
- Howk, J. C. 1999, *Ap&SS*, 269, 293, doi: [10.1023/A:1017032610206](https://doi.org/10.1023/A:1017032610206)
- Howk, J. C., & Savage, B. D. 1997, *AJ*, 114, 2463, doi: [10.1086/118660](https://doi.org/10.1086/118660)
- . 1999, *AJ*, 117, 2077, doi: [10.1086/300857](https://doi.org/10.1086/300857)
- Irwin, J. A., Kennedy, H., Parkin, T., & Madden, S. 2007, *A&A*, 474, 461, doi: [10.1051/0004-6361:20077729](https://doi.org/10.1051/0004-6361:20077729)
- Irwin, J. A., & Madden, S. C. 2006, *A&A*, 445, 123, doi: [10.1051/0004-6361:20053233](https://doi.org/10.1051/0004-6361:20053233)
- Kennicutt, R. C., & Evans, N. J. 2012, *ARA&A*, 50, 531, doi: [10.1146/annurev-astro-081811-125610](https://doi.org/10.1146/annurev-astro-081811-125610)
- Martig, M., Minchev, I., & Flynn, C. 2014, *MNRAS*, 442, 2474, doi: [10.1093/mnras/stu1003](https://doi.org/10.1093/mnras/stu1003)
- Meiksin, A. A. 2009, *RvMP*, 81, 1405, doi: [10.1103/RevModPhys.81.1405](https://doi.org/10.1103/RevModPhys.81.1405)
- Morrissey, P., Conrow, T., Barlow, T. A., et al. 2007, *ApJS*, 173, 682, doi: [10.1086/520512](https://doi.org/10.1086/520512)
- Popescu, C. C., Tuffs, R. J., Kylafis, N. D., & Madore, B. F. 2004, *A&A*, 414, 45, doi: [10.1051/0004-6361:20031581](https://doi.org/10.1051/0004-6361:20031581)
- Putman, M. E., Peek, J. E. G., & Joung, M. R. 2012, *ARA&A*, 50, 491, doi: [10.1146/annurev-astro-081811-125612](https://doi.org/10.1146/annurev-astro-081811-125612)
- Sandin, C. 2014, *A&A*, 567, A97, doi: [10.1051/0004-6361/201423429](https://doi.org/10.1051/0004-6361/201423429)
- . 2015, *A&A*, 577, A106, doi: [10.1051/0004-6361/201425168](https://doi.org/10.1051/0004-6361/201425168)
- Schechtman-Rook, A., Bershady, M. A., & Wood, K. 2012, *ApJ*, 746, 70, doi: [10.1088/0004-637X/746/1/70](https://doi.org/10.1088/0004-637X/746/1/70)
- Seon, K.-I., & Witt, A. N. 2012, *ApJ*, 758, 109, doi: [10.1088/0004-637X/758/2/109](https://doi.org/10.1088/0004-637X/758/2/109)
- Seon, K.-I., Witt, A. N., Shinn, J.-H., & Kim, I.-J. 2014, *ApJ*, 785, L18, doi: [10.1088/2041-8205/785/1/L18](https://doi.org/10.1088/2041-8205/785/1/L18)
- Sharma, S. 2017, *ARA&A*, 55, 213, doi: [10.1146/annurev-astro-082214-122339](https://doi.org/10.1146/annurev-astro-082214-122339)
- Shinn, J.-H., & Seon, K.-I. 2015, *ApJ*, 815, 133, doi: [10.1088/0004-637X/815/2/133](https://doi.org/10.1088/0004-637X/815/2/133)
- Spitzer, Jr., L. 1942, *ApJ*, 95, 329, doi: [10.1086/144407](https://doi.org/10.1086/144407)
- Steinacker, J., Baes, M., & Gordon, K. D. 2013, *ARA&A*, 51, 63, doi: [10.1146/annurev-astro-082812-141042](https://doi.org/10.1146/annurev-astro-082812-141042)
- Storn, R., & Price, K. 1997, *J. Global Optim.*, 11, 341, doi: [10.1023/A:1008202821328](https://doi.org/10.1023/A:1008202821328)
- Thompson, T. W. J., Howk, J. C., & Savage, B. D. 2004, *AJ*, 128, 662, doi: [10.1086/422485](https://doi.org/10.1086/422485)
- Veilleux, S., Cecil, G., & Bland-Hawthorn, J. 2005, *ARA&A*, 43, 769, doi: [10.1146/annurev.astro.43.072103.150610](https://doi.org/10.1146/annurev.astro.43.072103.150610)
- Wainscoat, R. J., Cohen, M., Volk, K., Walker, H. J., & Schwartz, D. E. 1992, *ApJS*, 83, 111, doi: [10.1086/191733](https://doi.org/10.1086/191733)
- Xilouris, E. M., Byun, Y. I., Kylafis, N. D., Paleologou, E. V., & Papamastorakis, J. 1999, *A&A*, 344, 868
- Xilouris, E. M., Kylafis, N. D., Papamastorakis, J., Paleologou, E. V., & Haerendel, G. 1997, *A&A*, 325, 135
- York, D. G., Adelman, J., Anderson, Jr., J. E., et al. 2000, *AJ*, 120, 1579, doi: [10.1086/301513](https://doi.org/10.1086/301513)

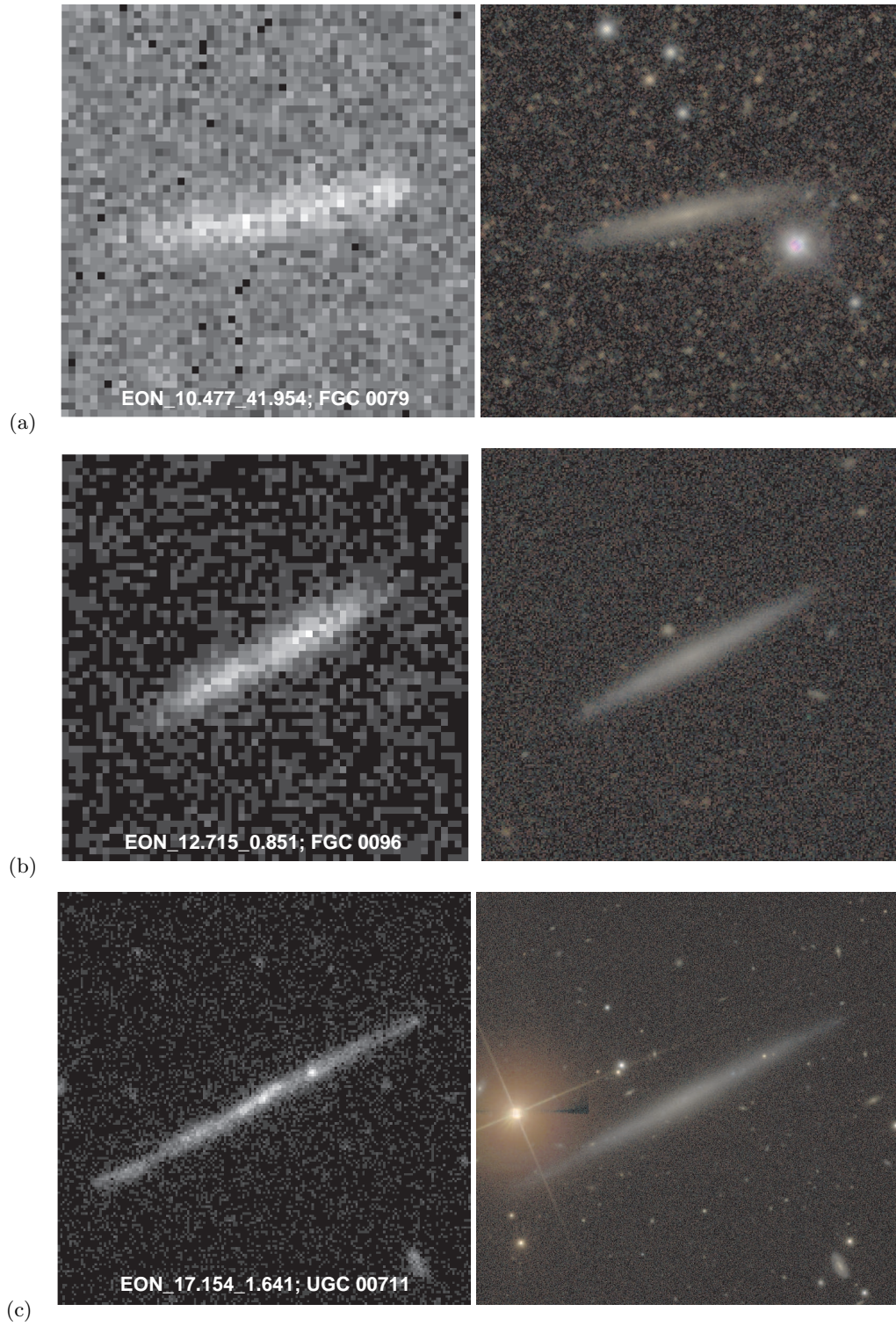


Figure 1. *GALEX* FUV images (*left*) and *SDSS* RGB images (*right*) of the 23 target edge-on galaxies. The *SDSS* RGB image is made from g =blue, r =green, and i =red. The *GALEX* image field-of-view is the same with the one in Fig. 5-27.

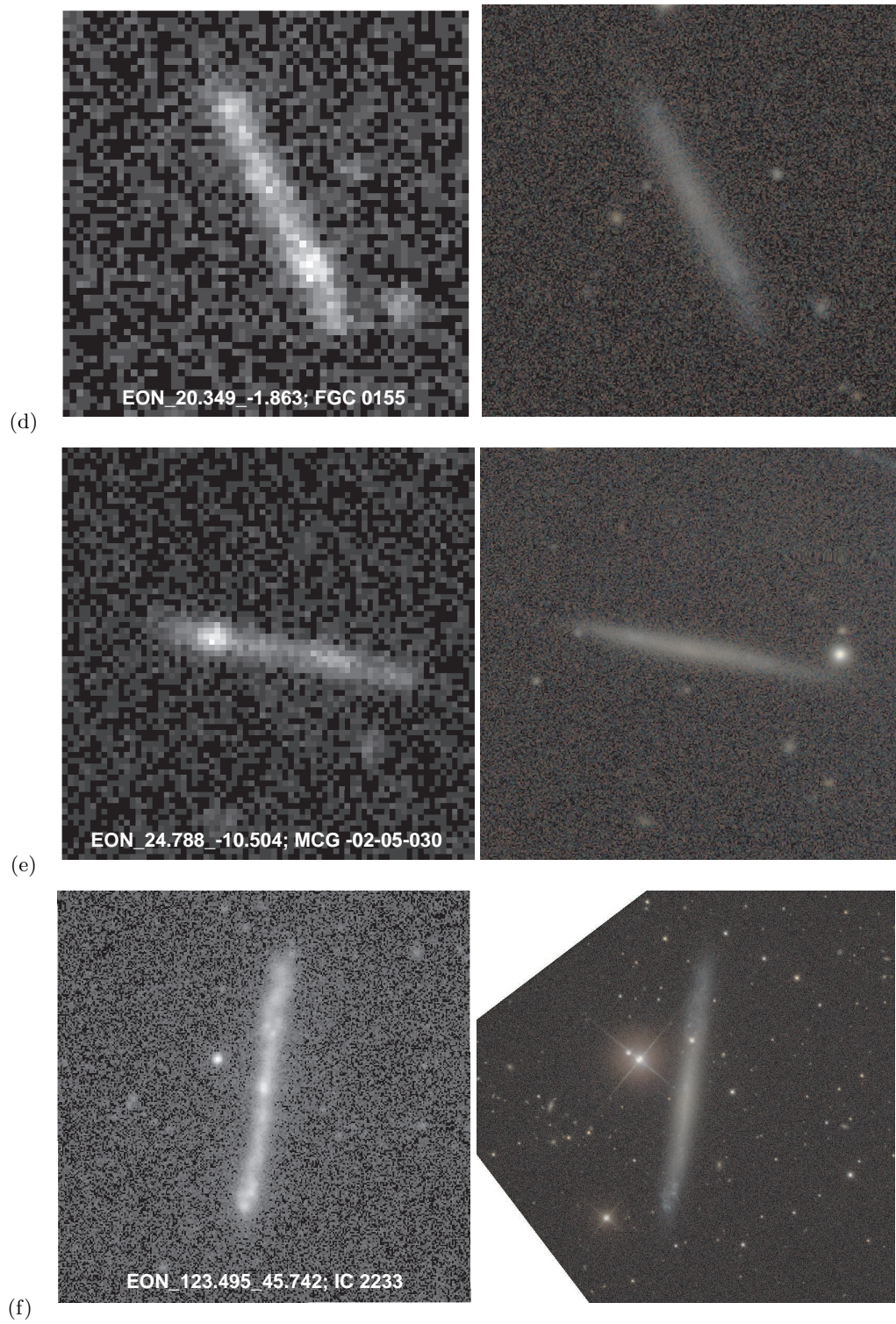


Figure 1. Continued.



Figure 1. Continued.

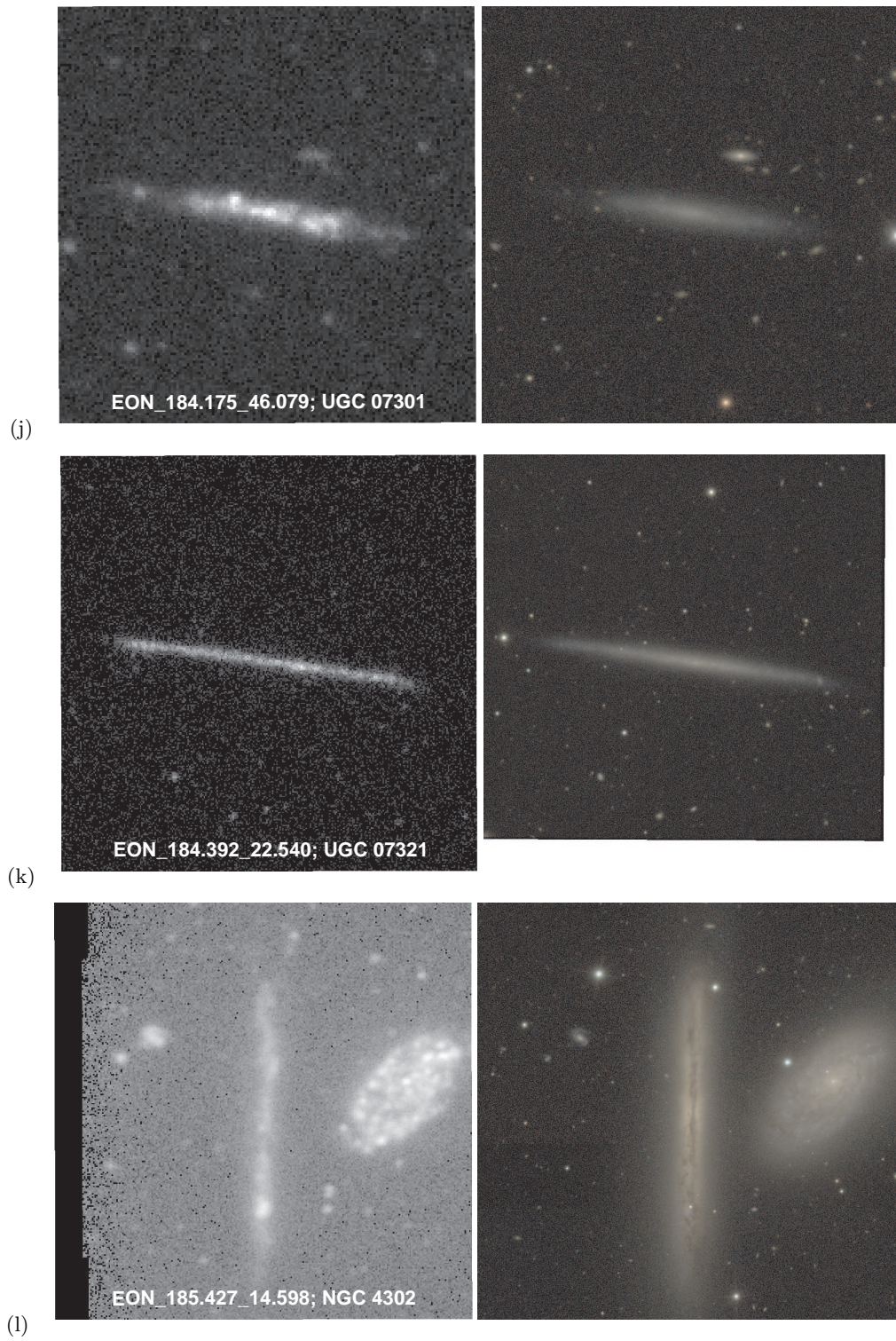


Figure 1. Continued.

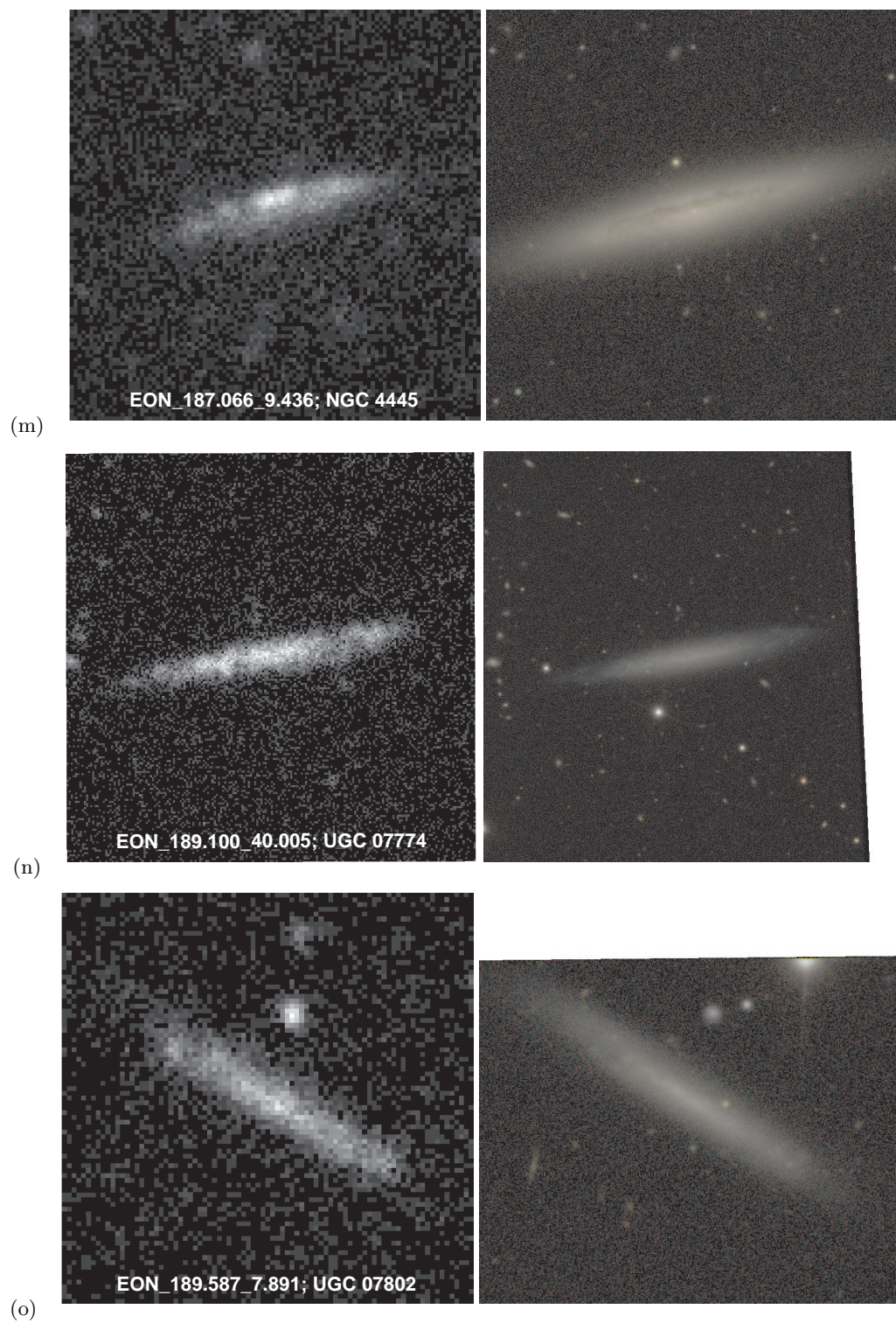


Figure 1. Continued.

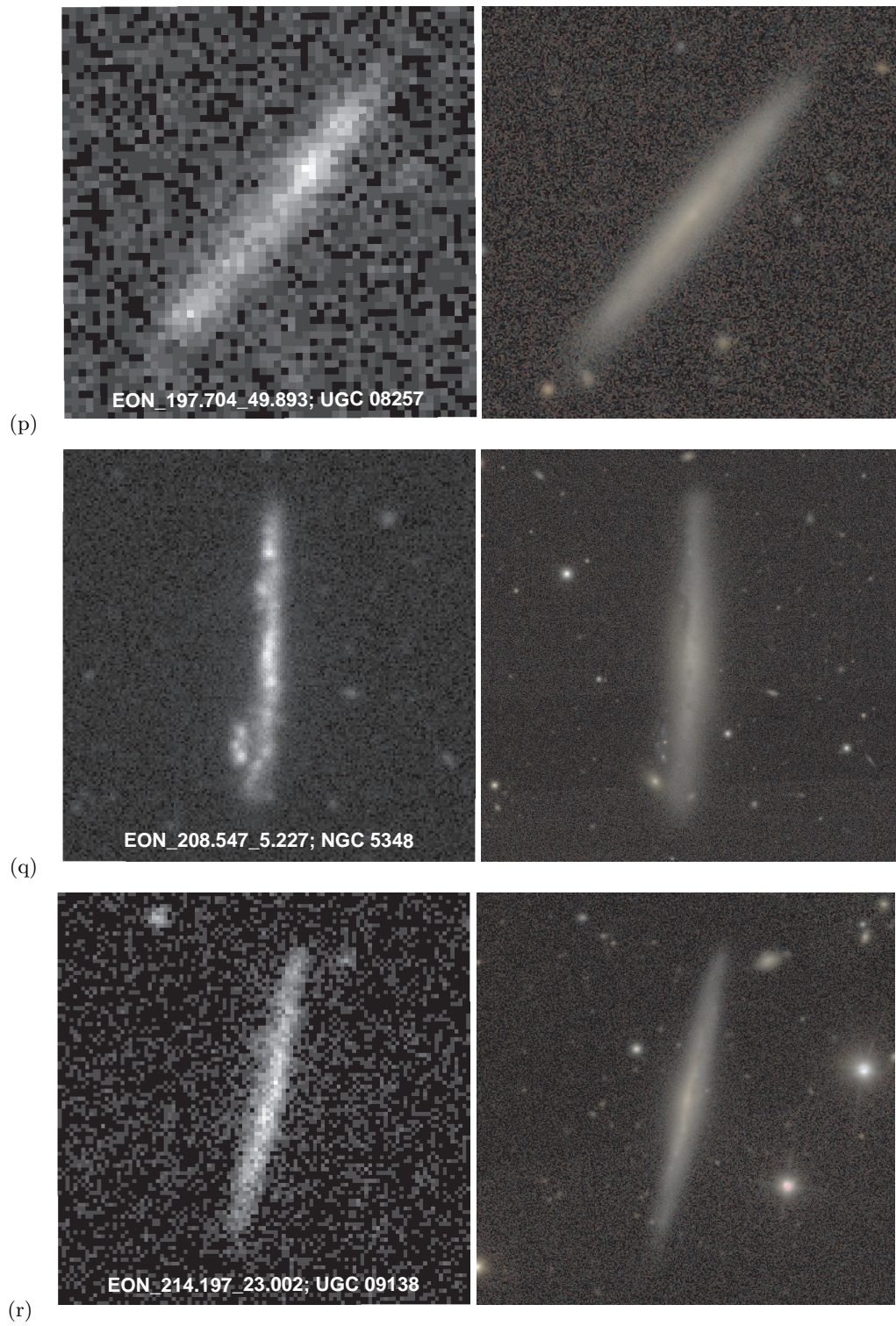


Figure 1. Continued.

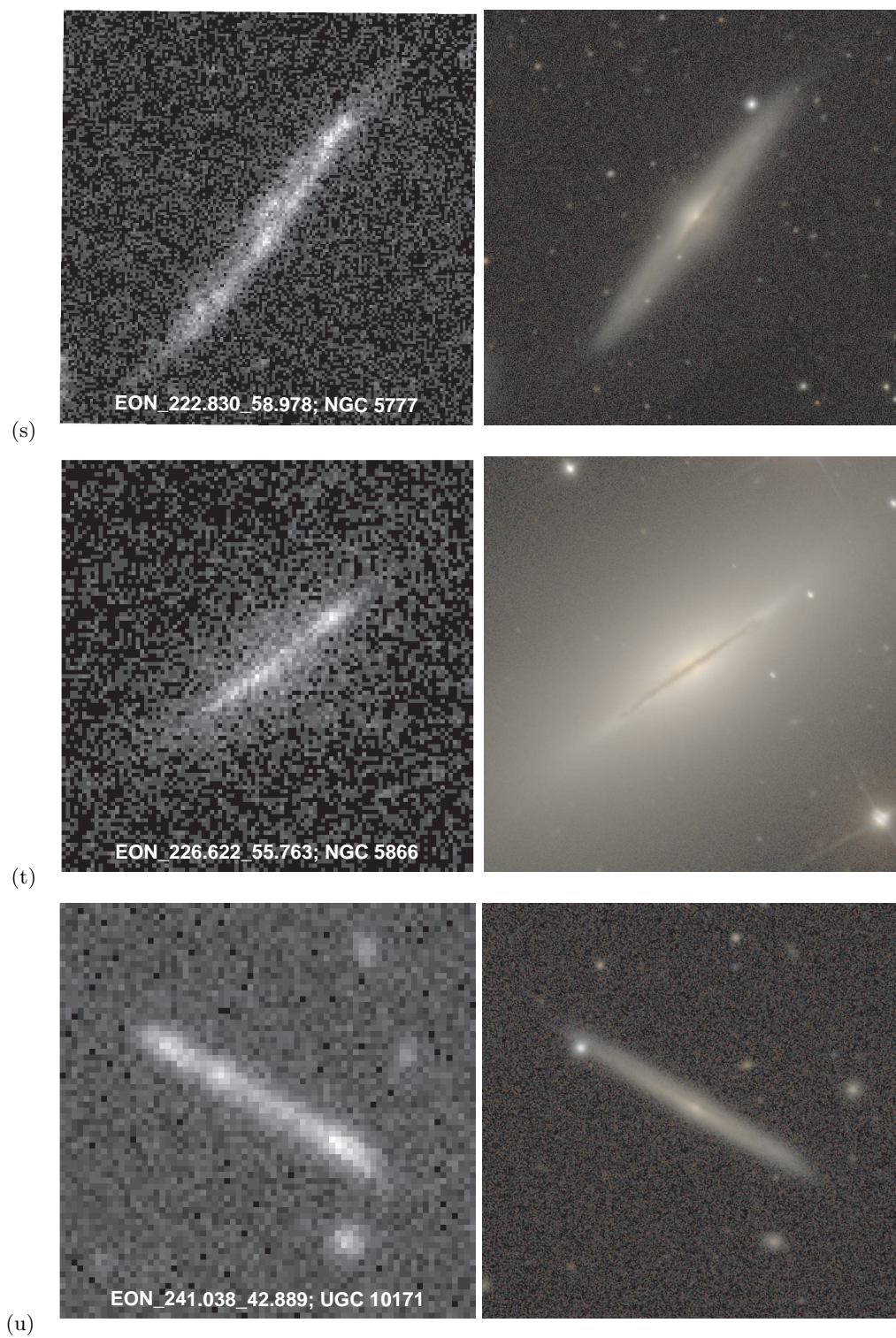


Figure 1. Continued.

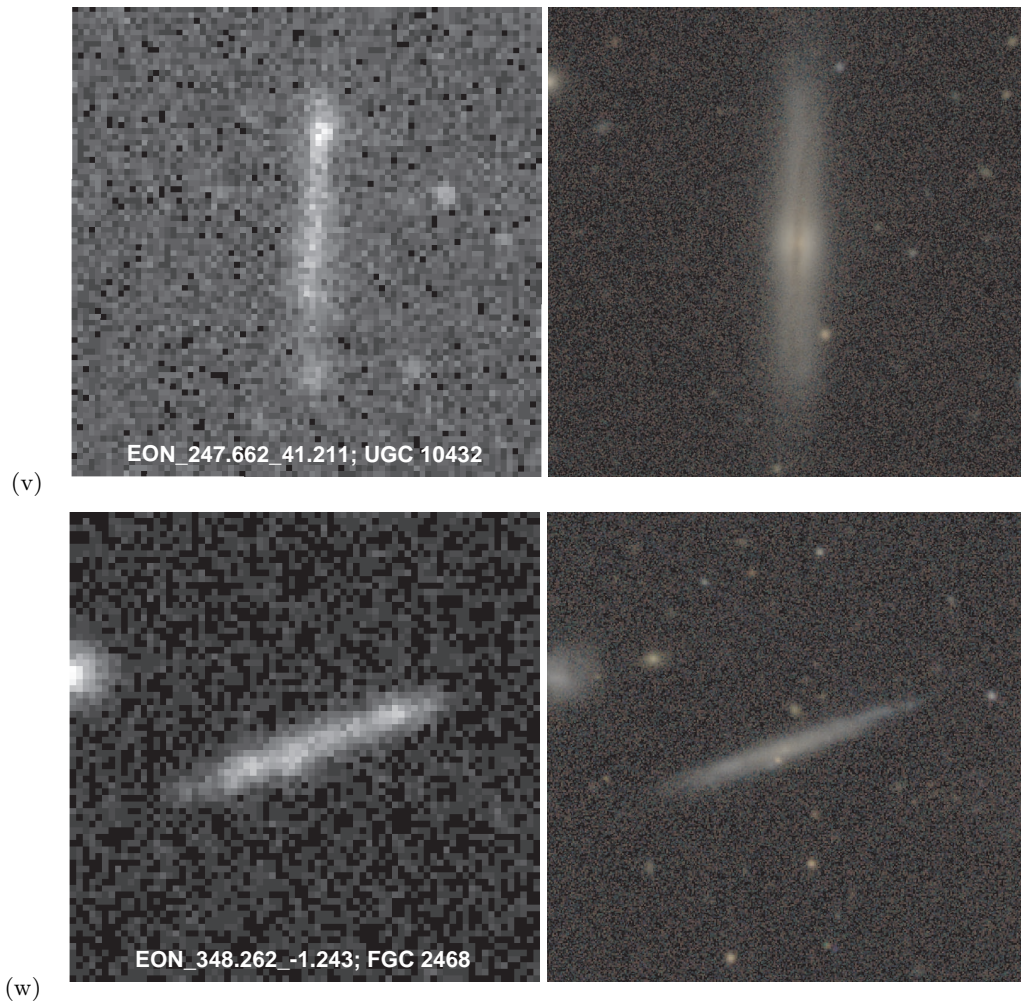


Figure 1. Continued.

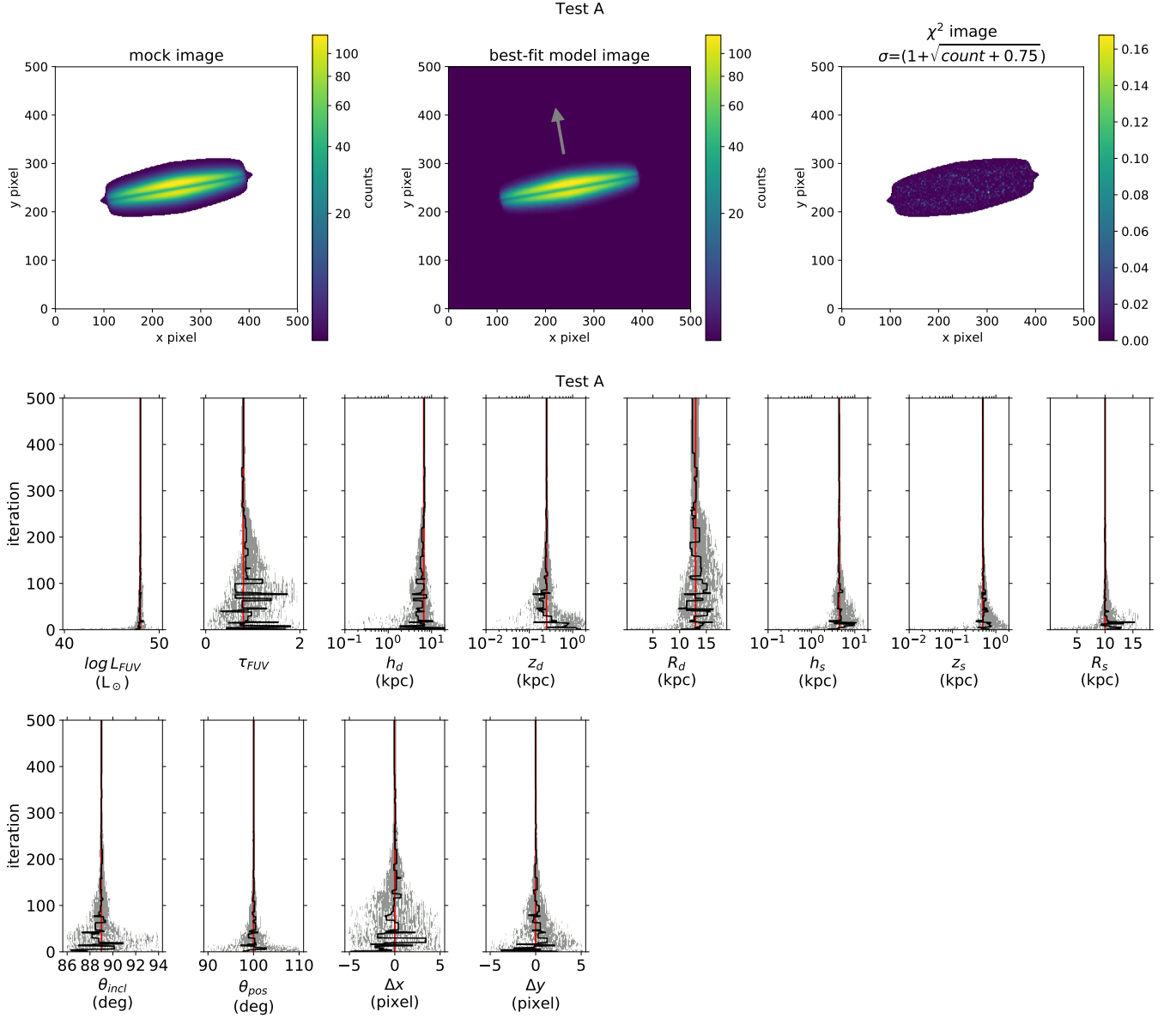


Figure 2. The results of Test A. The three *top panels* show the mock observation image, best-fit model image, and the goodness of fit image from left to right, respectively. See text for the definition of the goodness of fit image. The white areas are excluded from the model fitting. The gray arrow on the best-fit model image is to define the inclination angle which increases from the arrow to the direction into the page. The *middle and bottom panels* show the evolution of fitting parameters over the iteration. The eight *middle panels* are for the intrinsic galactic structural parameters, while the four *bottom panels* are for the viewpoints. The *gray points* indicate the parameter values of the population. The *black line* shows the evolution of the best-fit parameter along the iteration. The *red vertical lines* indicate the model input values.

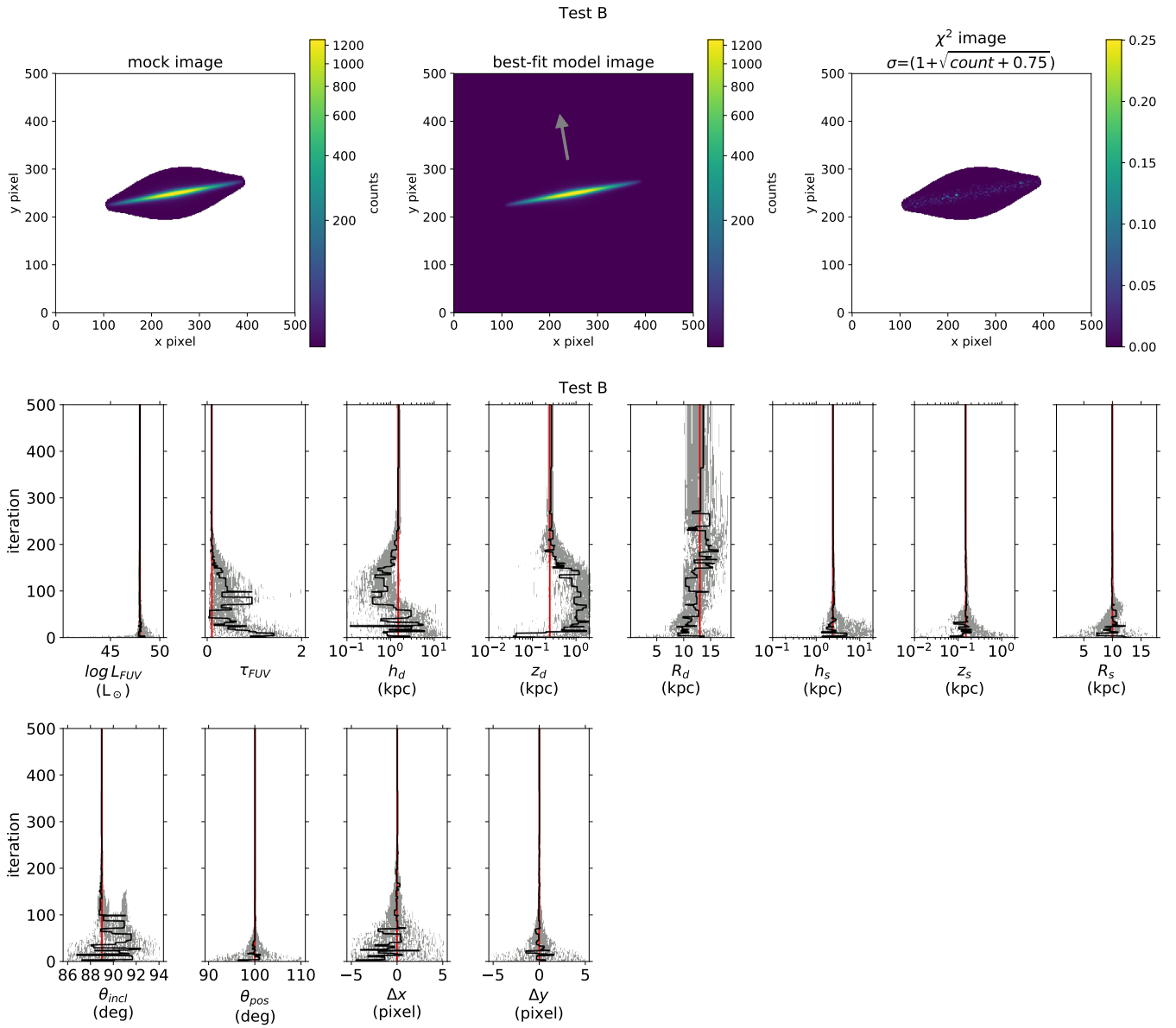


Figure 3. The results of Test B. The rest are the same with Fig. 2

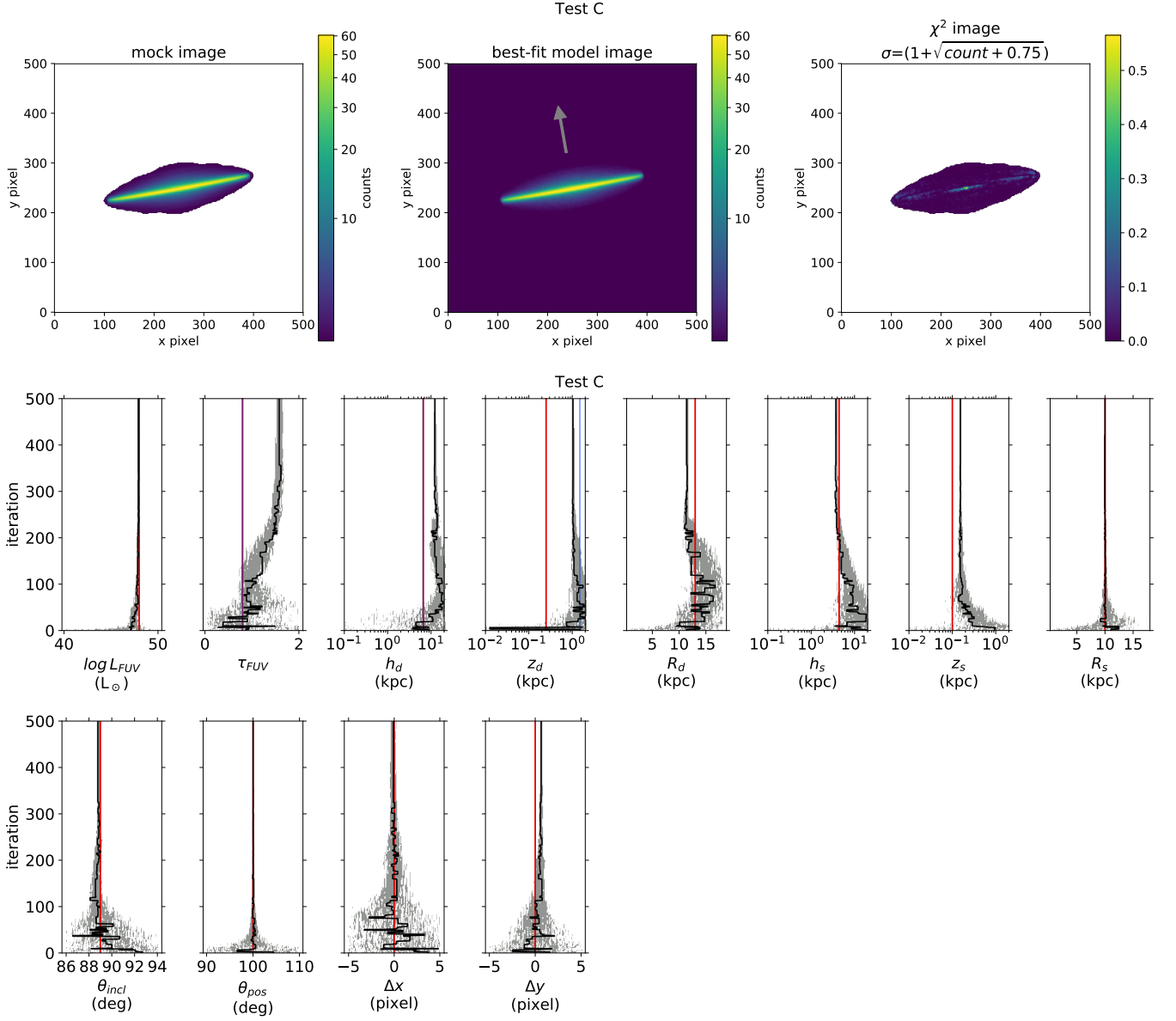


Figure 4. The results of Test C. The *blue vertical lines* are additionally displayed to indicate the second (thick) dust component (see text). In the case of τ_{FUV} and h_d , the red and blue lines are overlapped because we adopted the same τ_{FUV} and h_d values for the two dust components. The rest are the same with Fig. 2

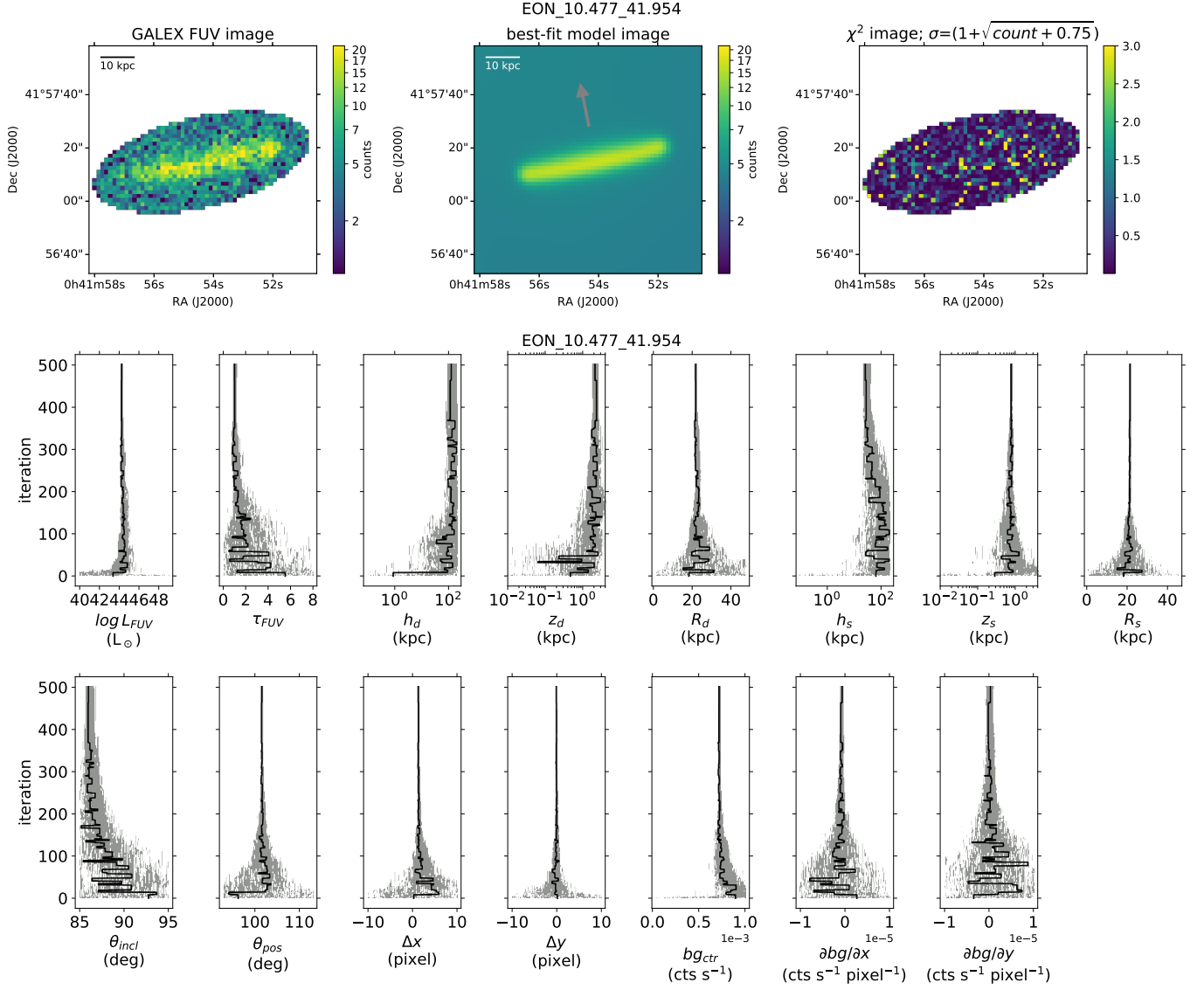


Figure 5. Fitting results for EON_10.477_41.954. The three *top panels* show the *GALEX FUV count* image, best-fit model image, and the goodness of fit image from left to right, respectively. The colorbar maximum is set as 3 in the goodness of fit image. The white areas are excluded from the model fitting. The gray arrow on the best-fit model image is to define the inclination angle which increases from the arrow to the direction into the page. The *middle and bottom panels* show the evolution of fitting parameters over the iteration. The eight *middle panels* are for the galactic structural parameters, while the seven *bottom panels* are for the viewpoints and the background. The *gray points* indicate the parameter values of the population. The *black line* shows the evolution of the best-fit parameter along the iteration.

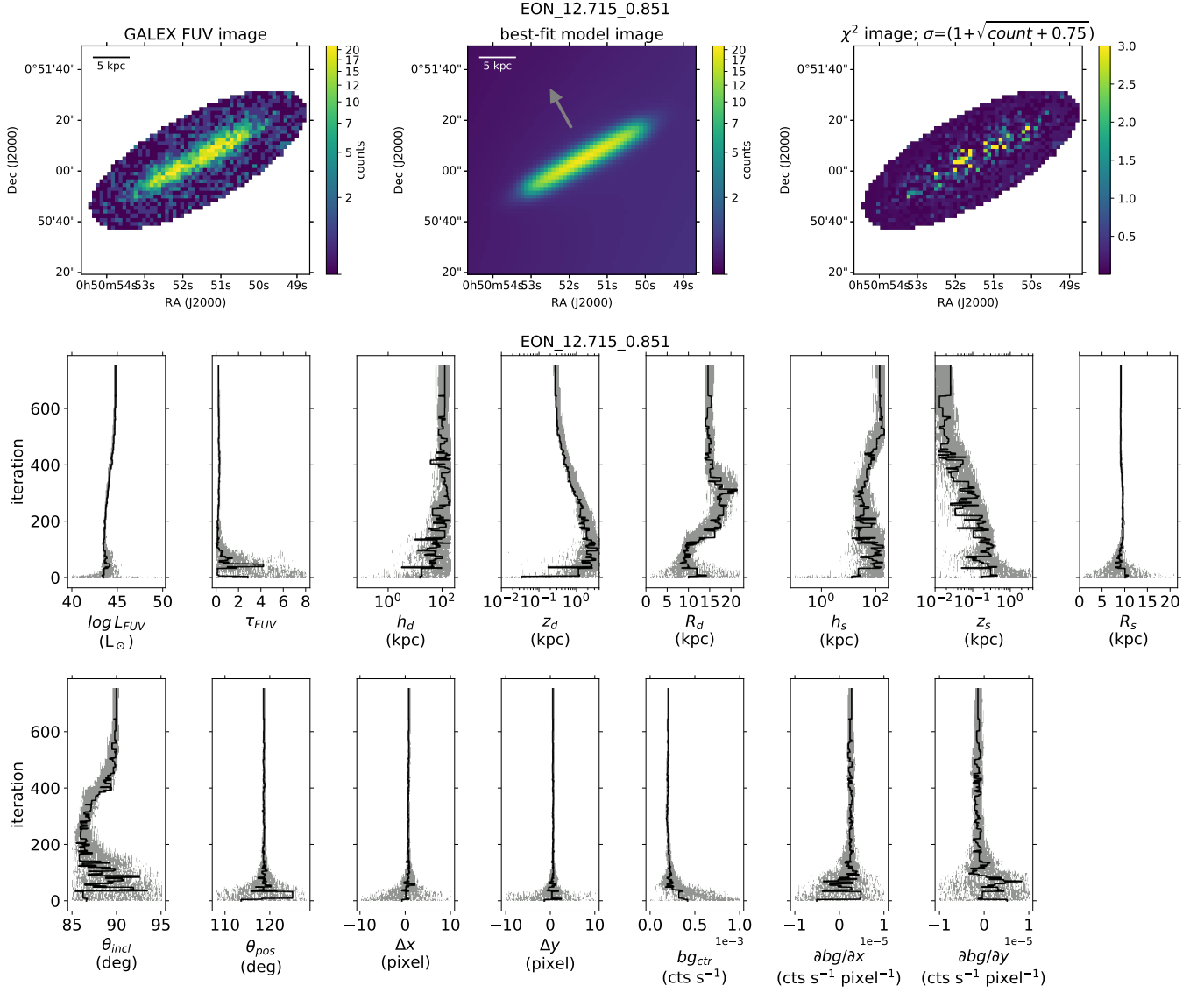


Figure 6. Fitting results for EON_12.715_0.851. The rest are the same as in Fig. 5

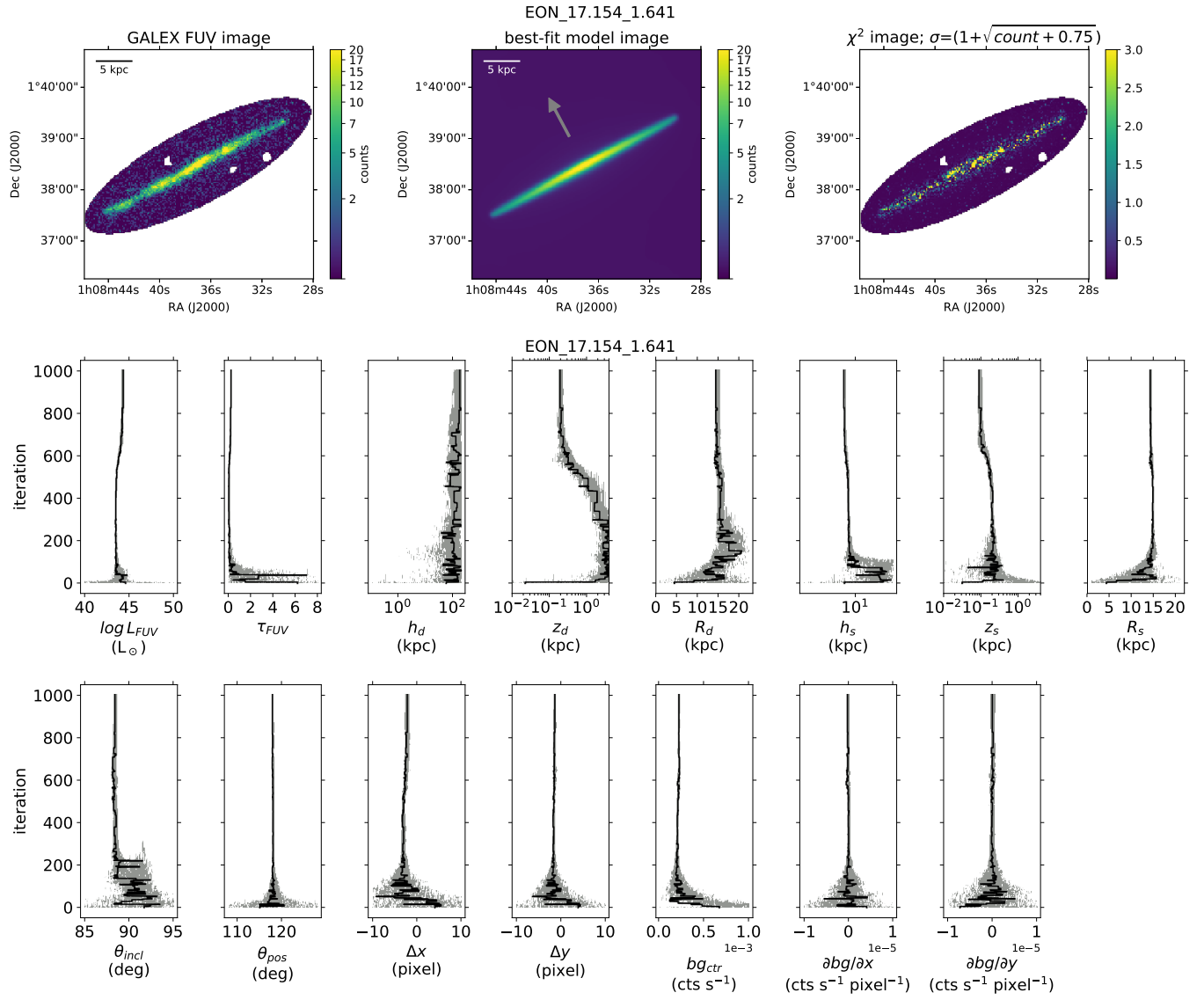


Figure 7. Fitting results for EON_17.154.1.641. The rest are the same as in Fig. 5

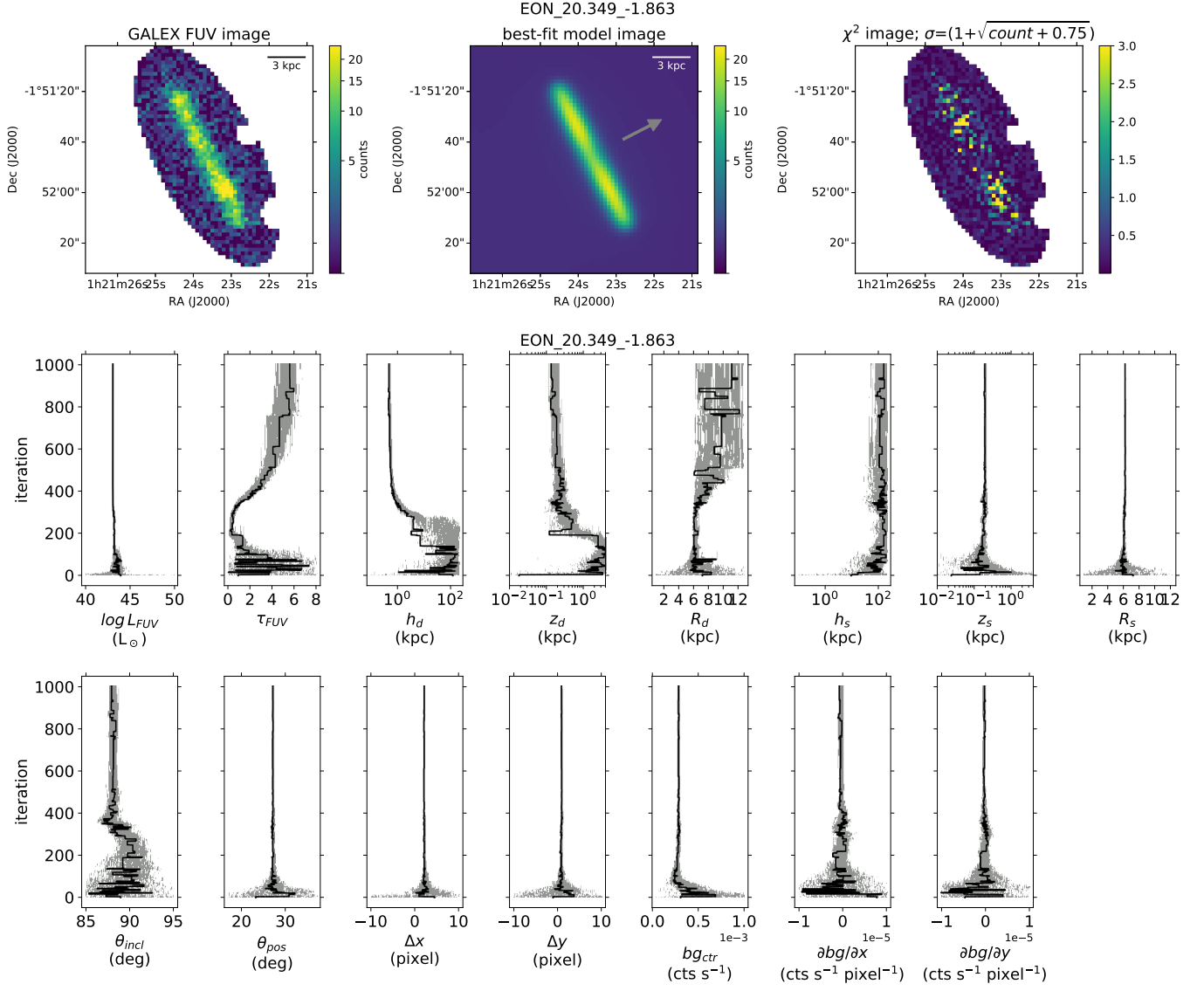


Figure 8. Fitting results for EON_20.349_-1.863. The rest are the same as in Fig. 5

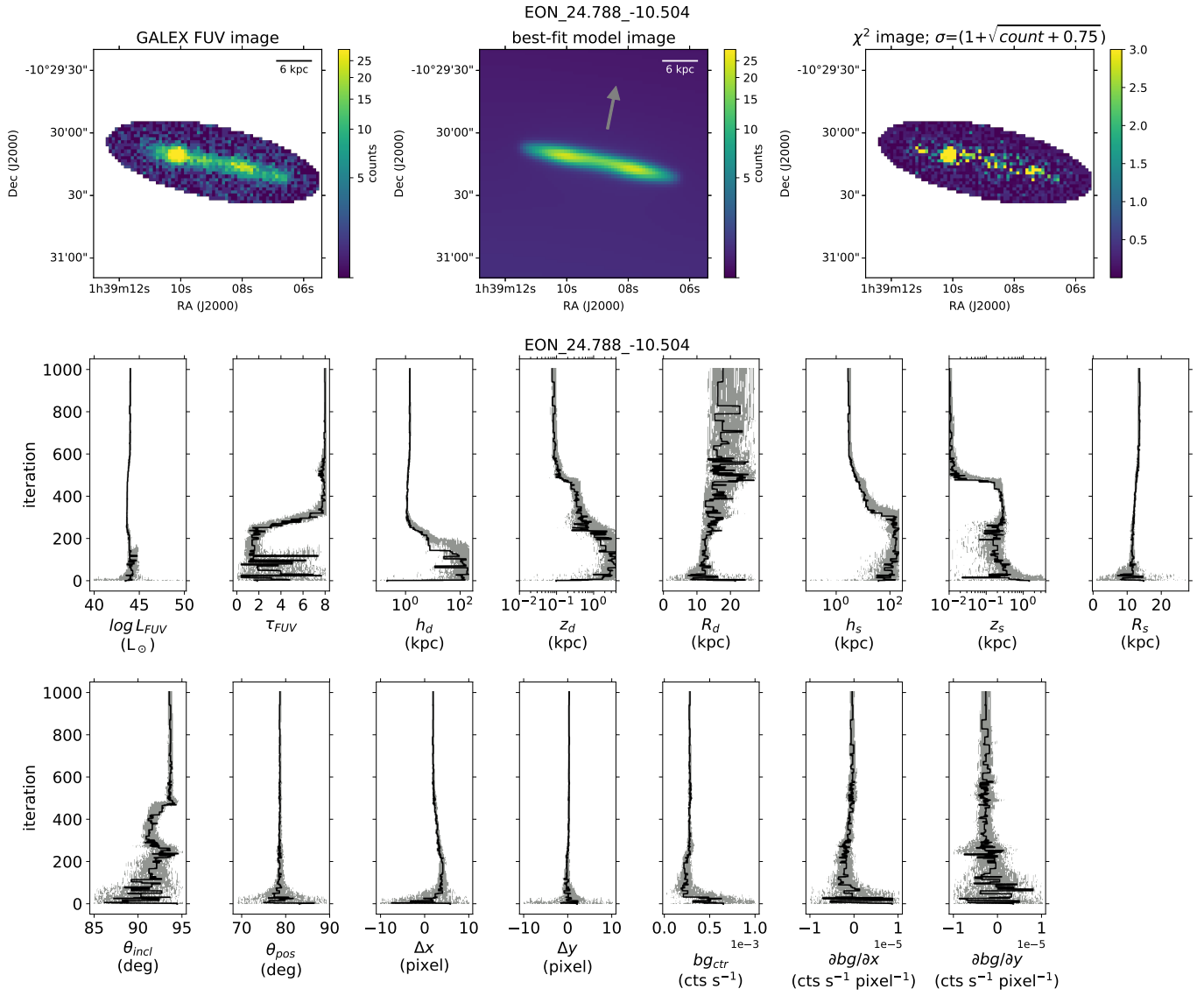


Figure 9. Fitting results for EON_24.788_-10.504. The rest are the same as in Fig. 5

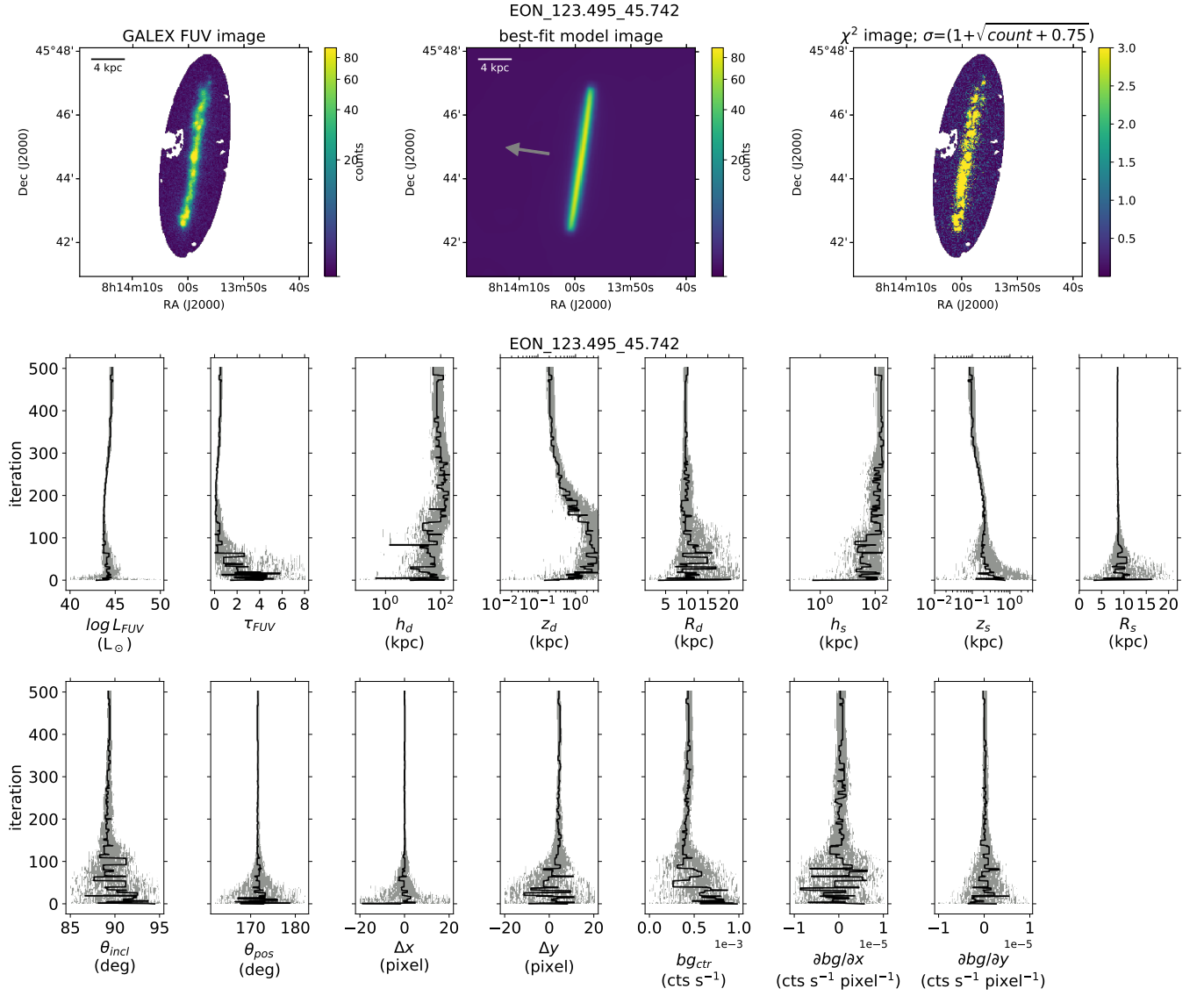


Figure 10. Fitting results for EON_123.495_45.742. The rest are the same as in Fig. 5

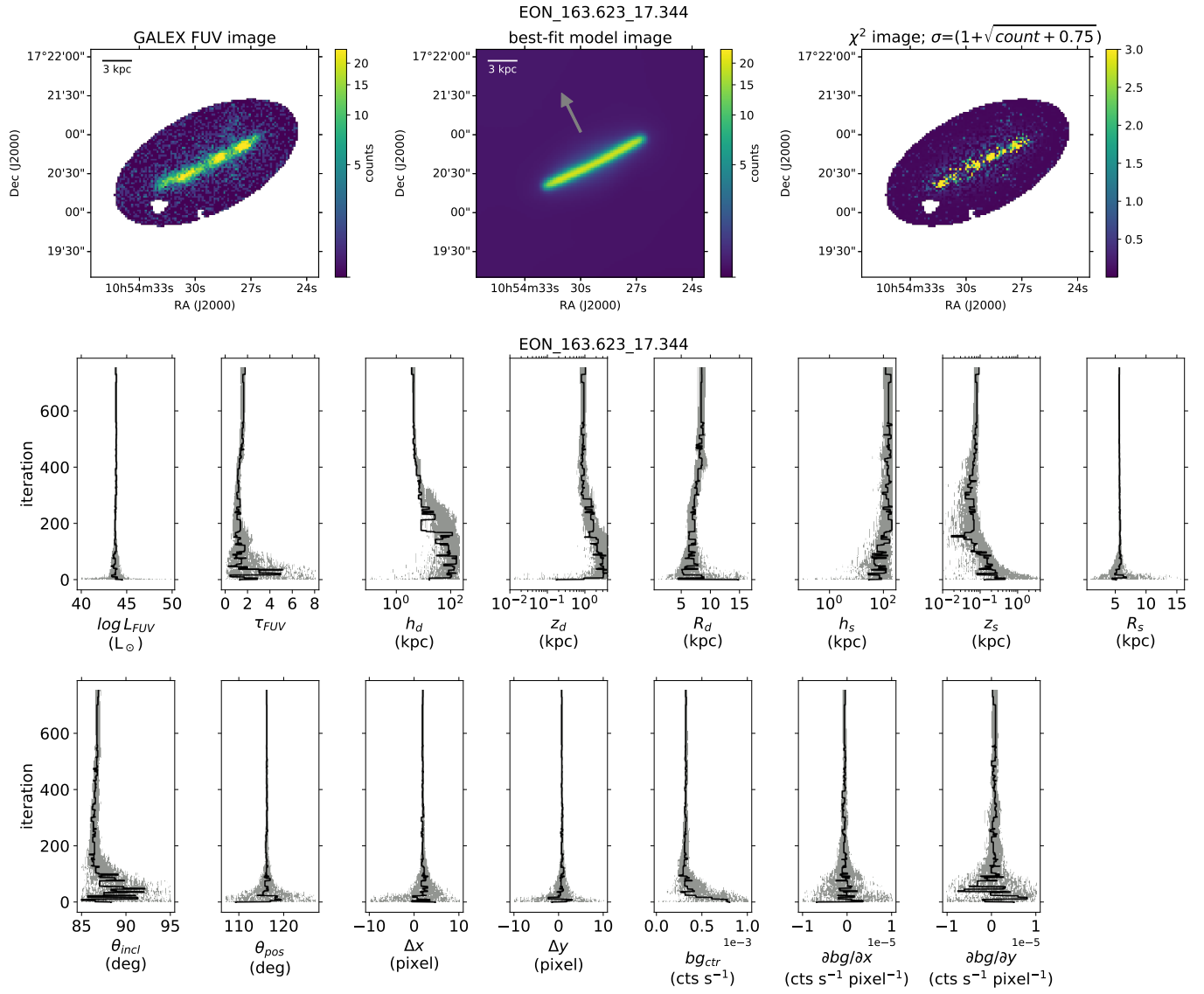


Figure 11. Fitting results for EON_163.623_17.344. The rest are the same as in Fig. 5

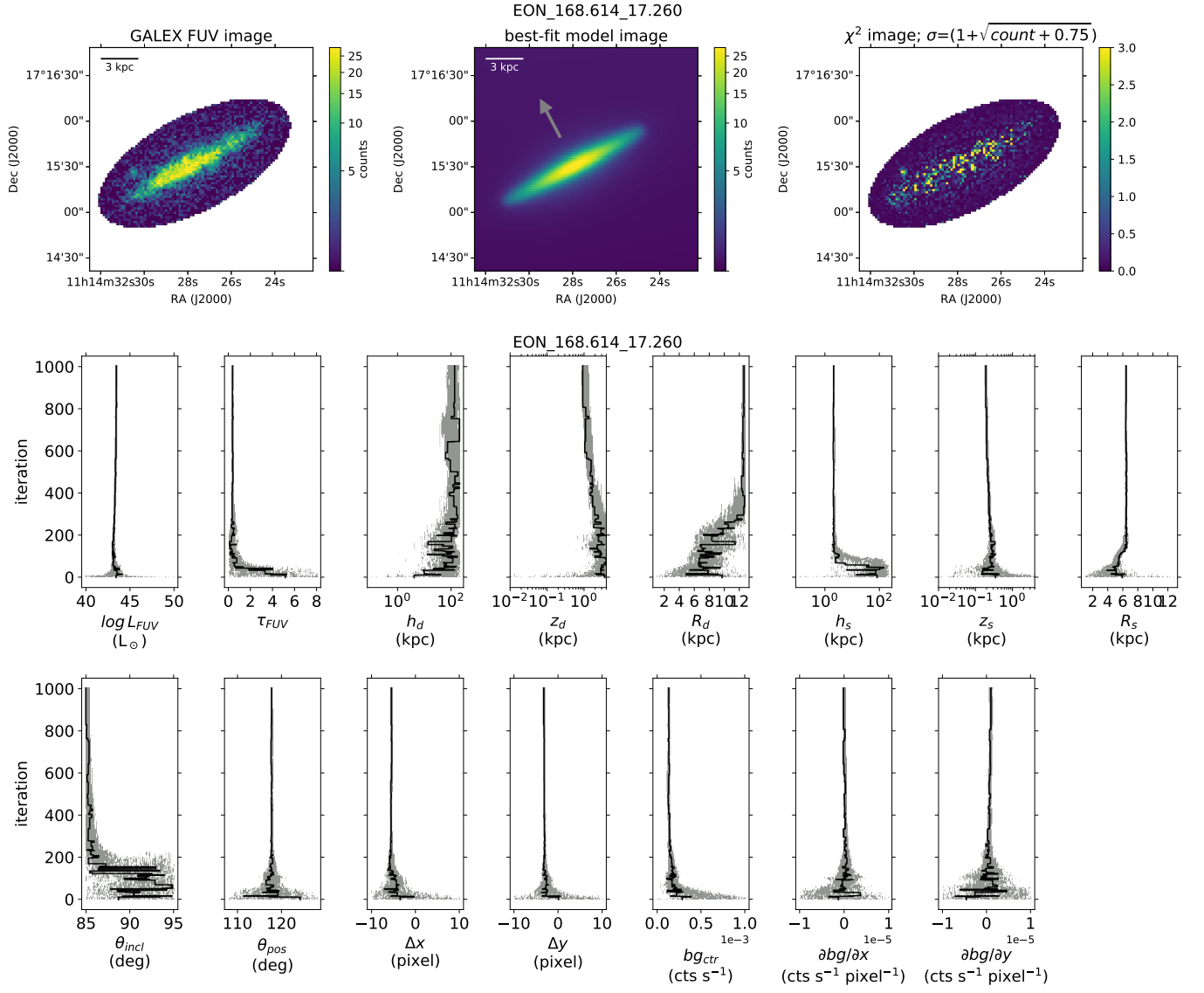


Figure 12. Fitting results for EON_168.614_17.260. The rest are the same as in Fig. 5

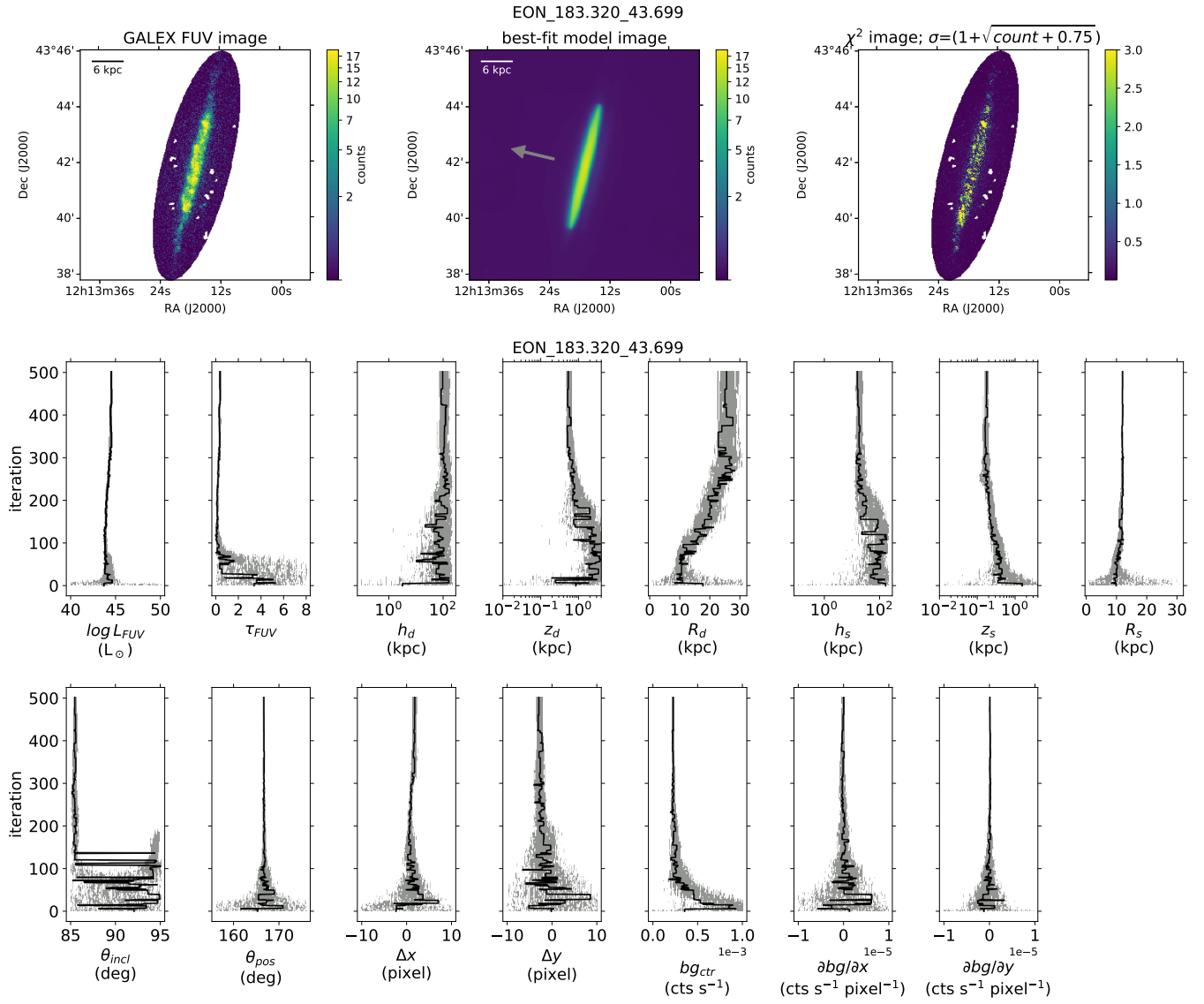


Figure 13. Fitting results for EON_183.320_43.699. The rest are the same as in Fig. 5

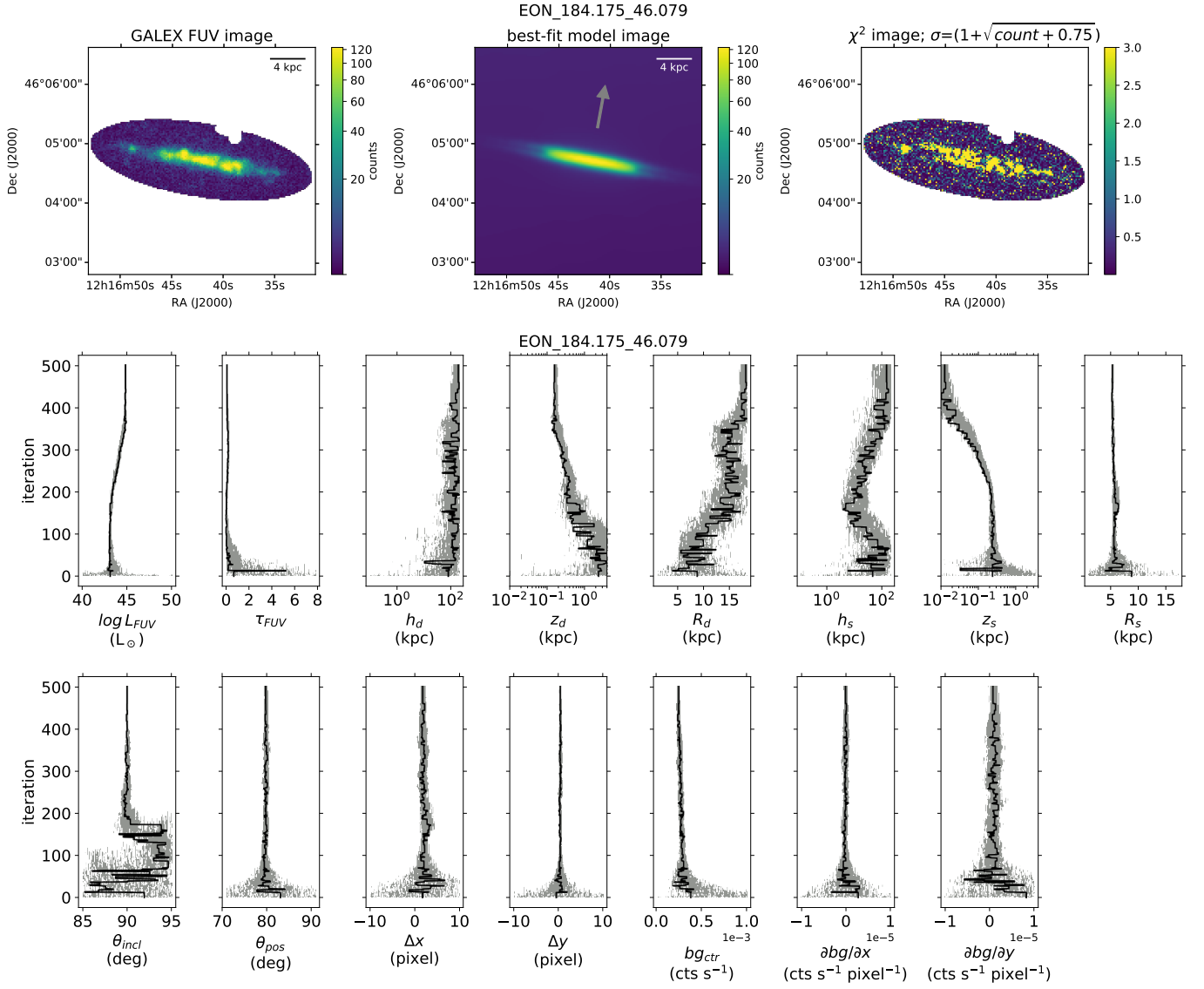


Figure 14. Fitting results for EON_184.175_46.079. The rest are the same as in Fig. 5

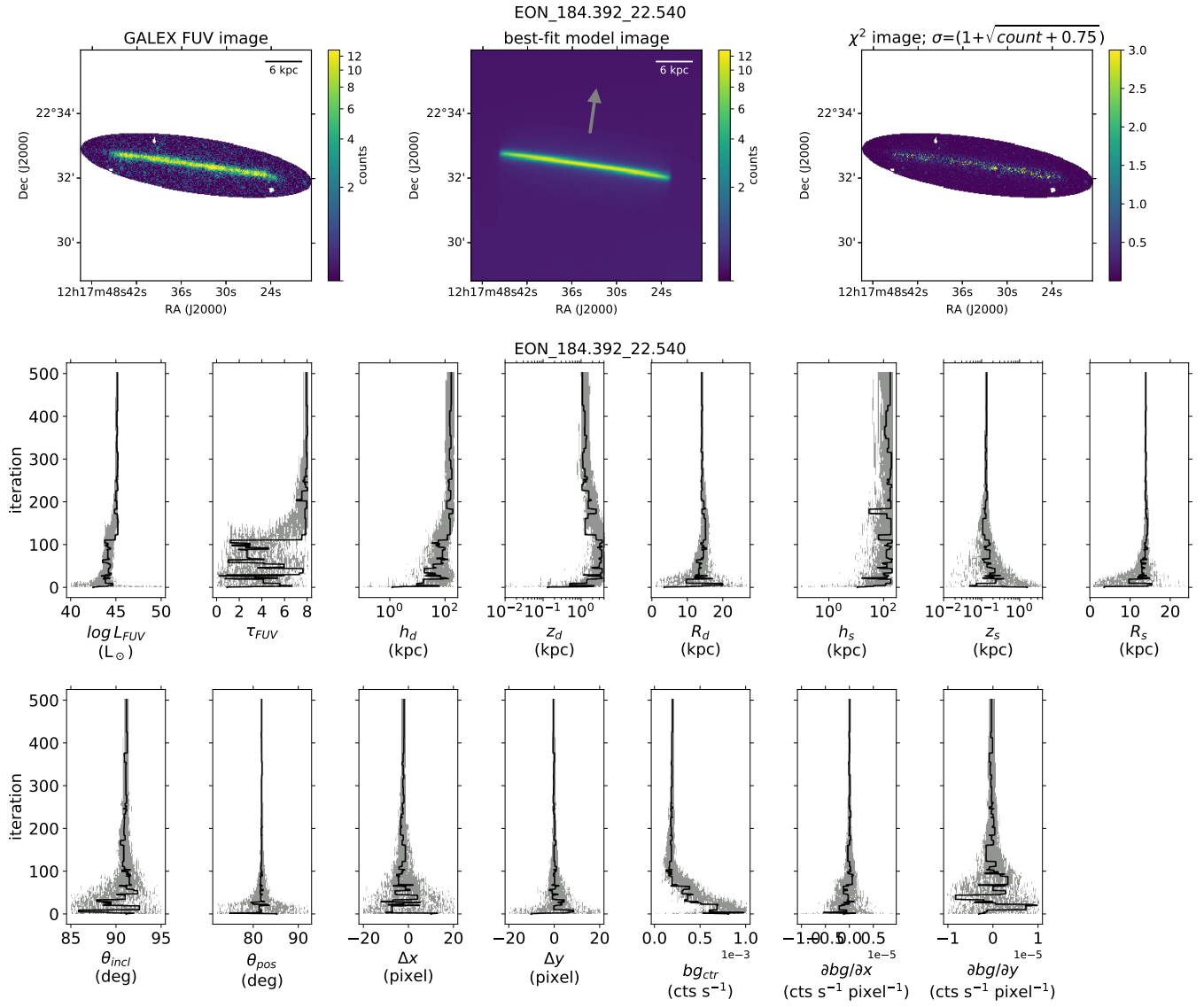


Figure 15. Fitting results for EON_184.392_22.540. The rest are the same as in Fig. 5

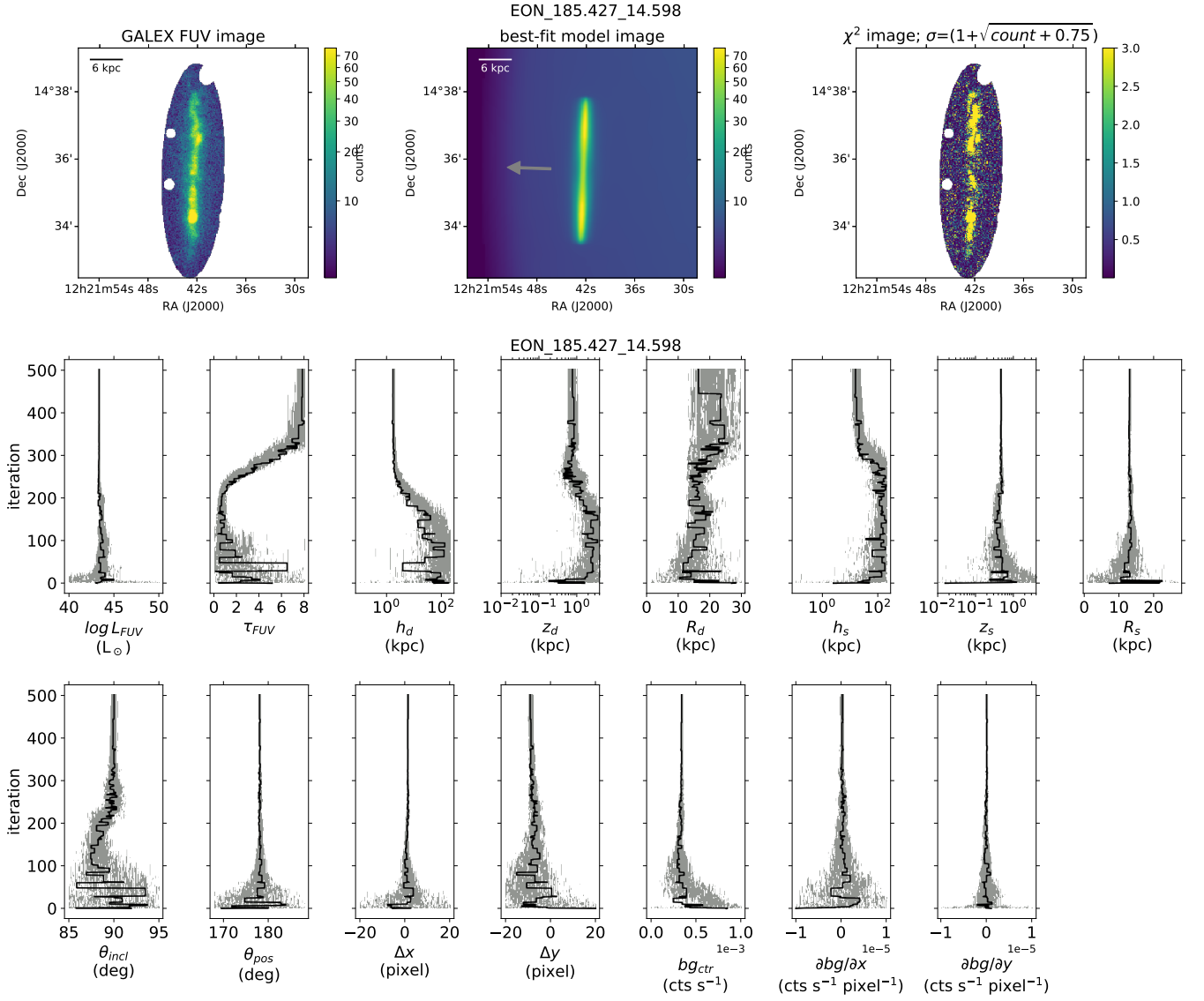


Figure 16. Fitting results for EON_185.427_14.598. The rest are the same as in Fig. 5

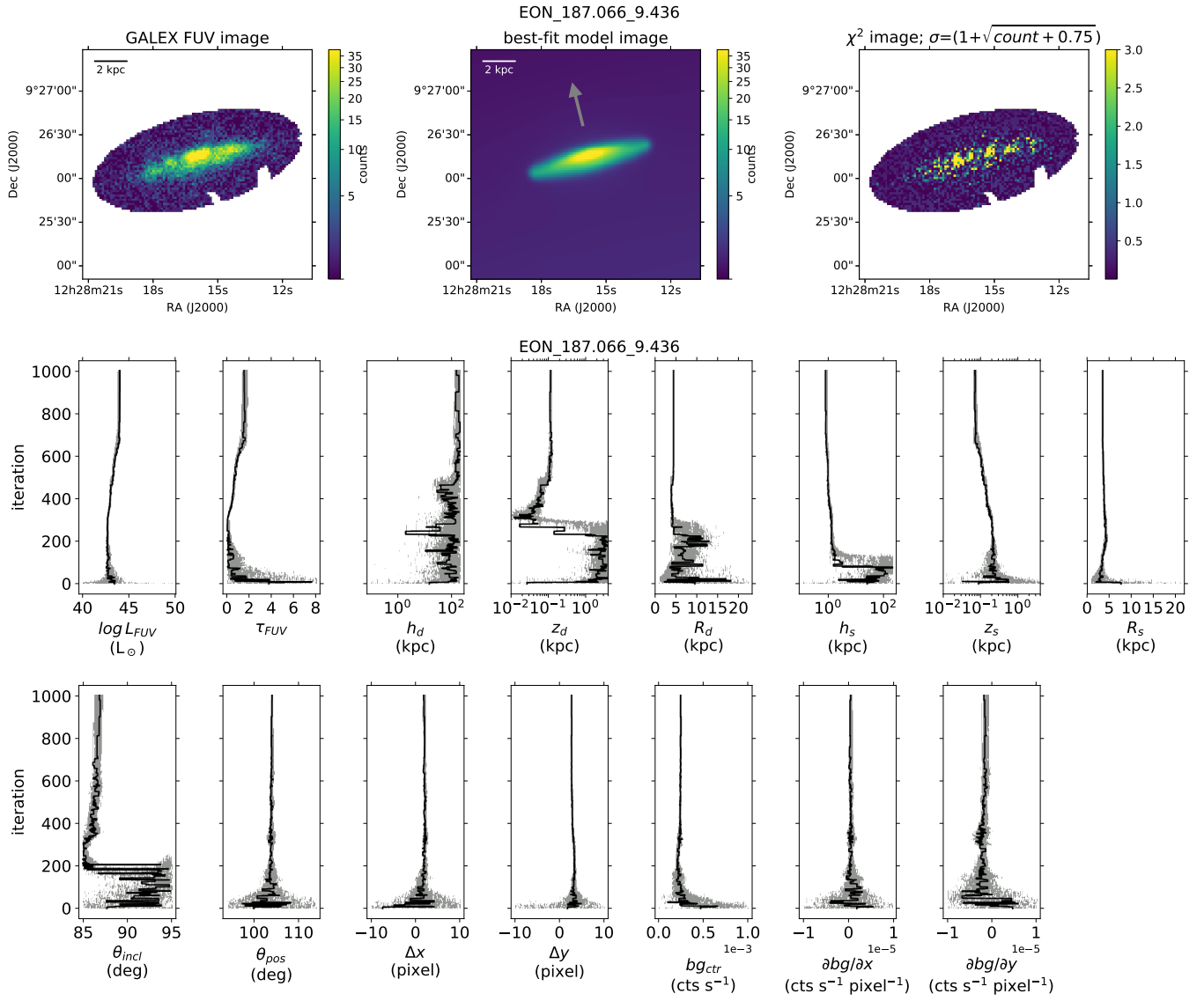


Figure 17. Fitting results for EON_187.066_9.436. The rest are the same as in Fig. 5

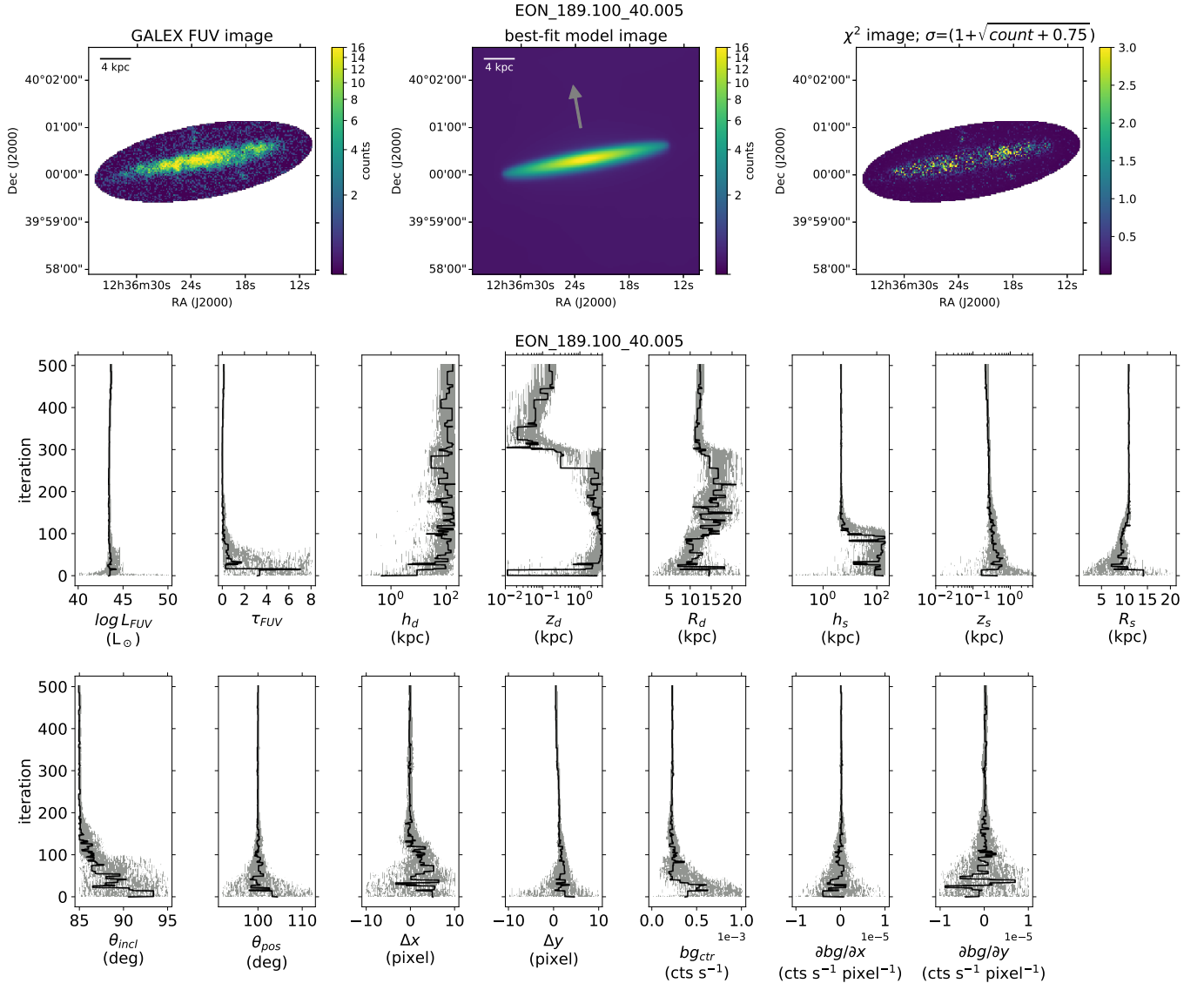


Figure 18. Fitting results for EON_189.100_40.005. The rest are the same as in Fig. 5

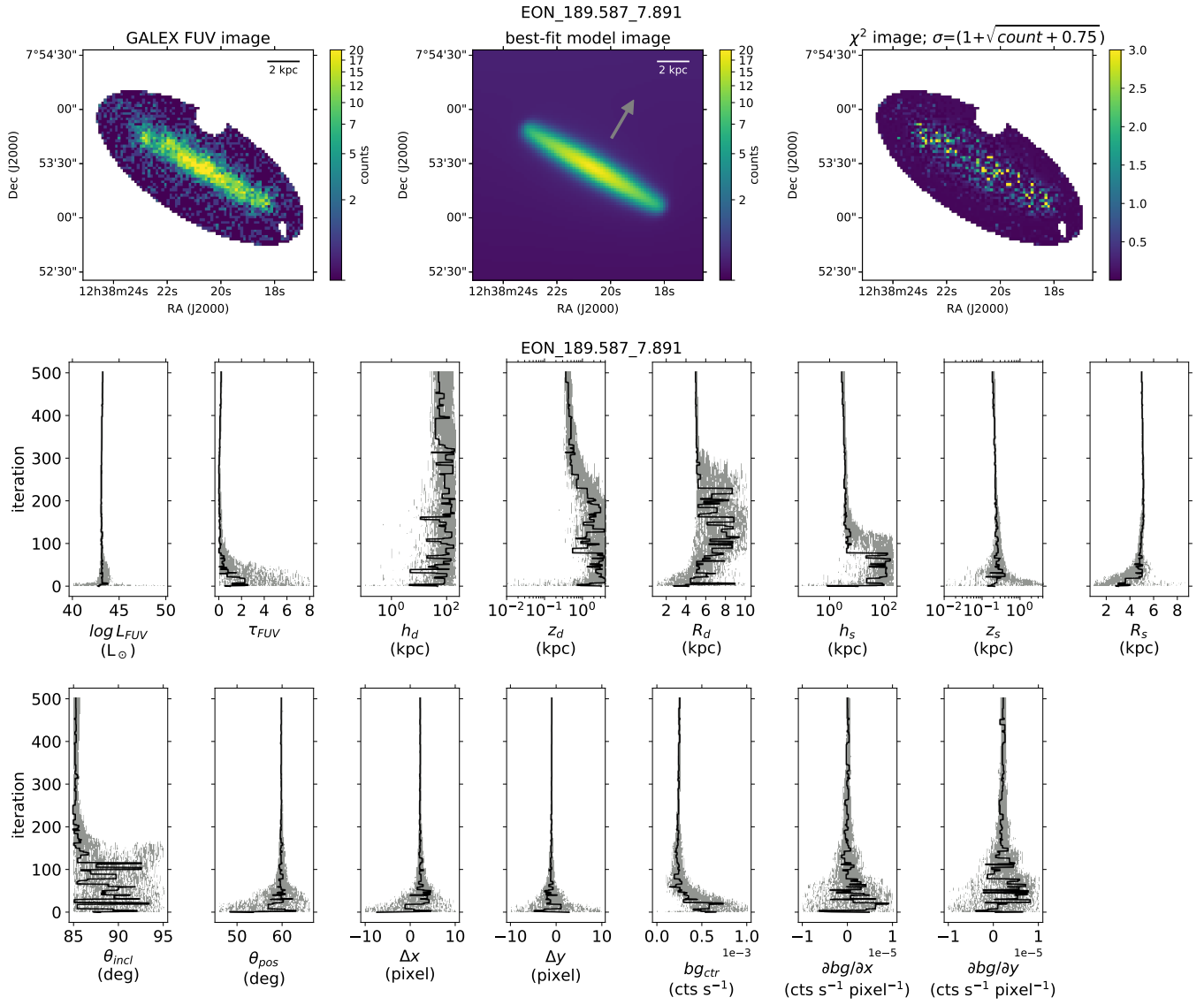


Figure 19. Fitting results for EON_189.587_7.891. The rest are the same as in Fig. 5

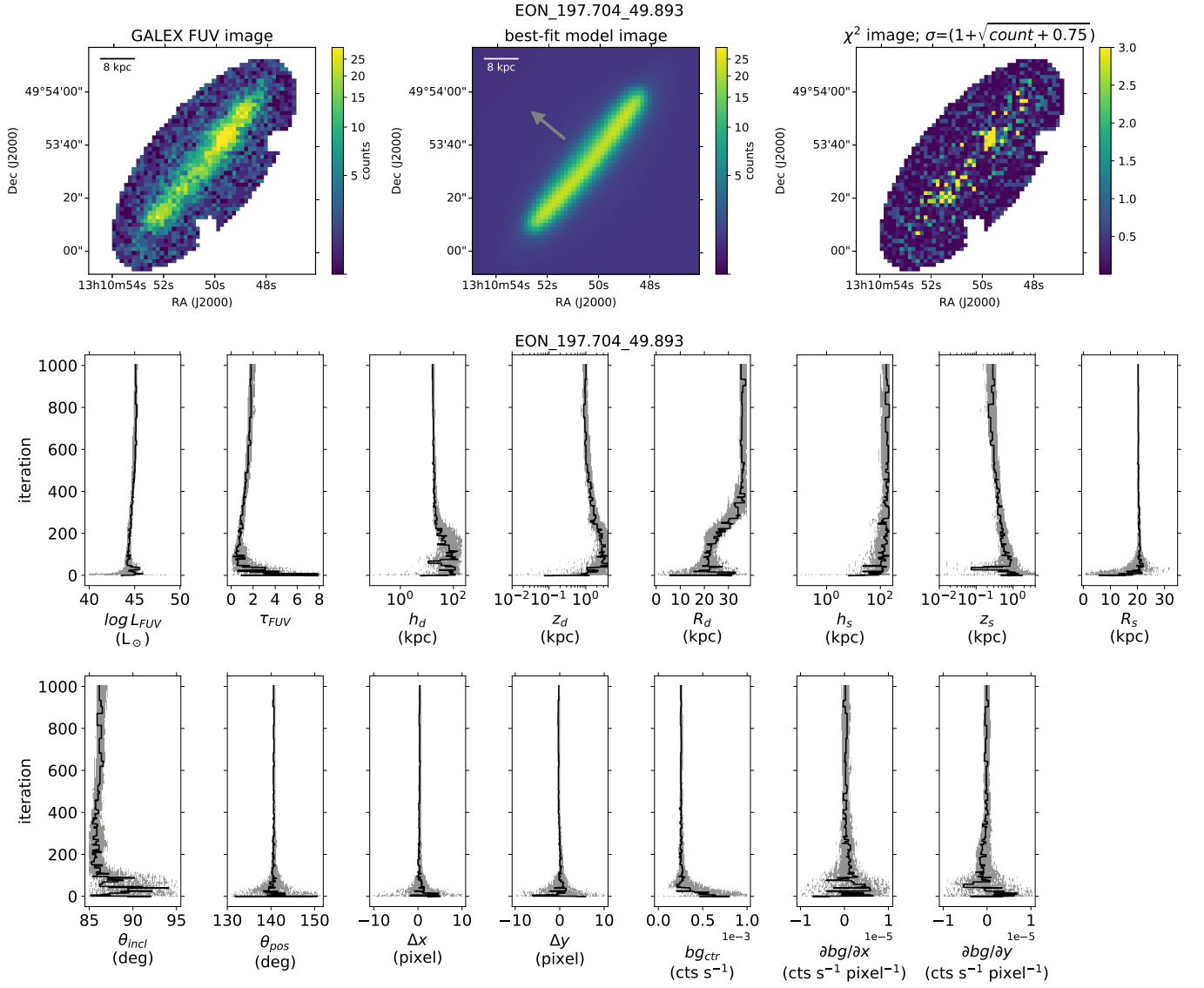


Figure 20. Fitting results for EON_197.704_49.893. The rest are the same as in Fig. 5

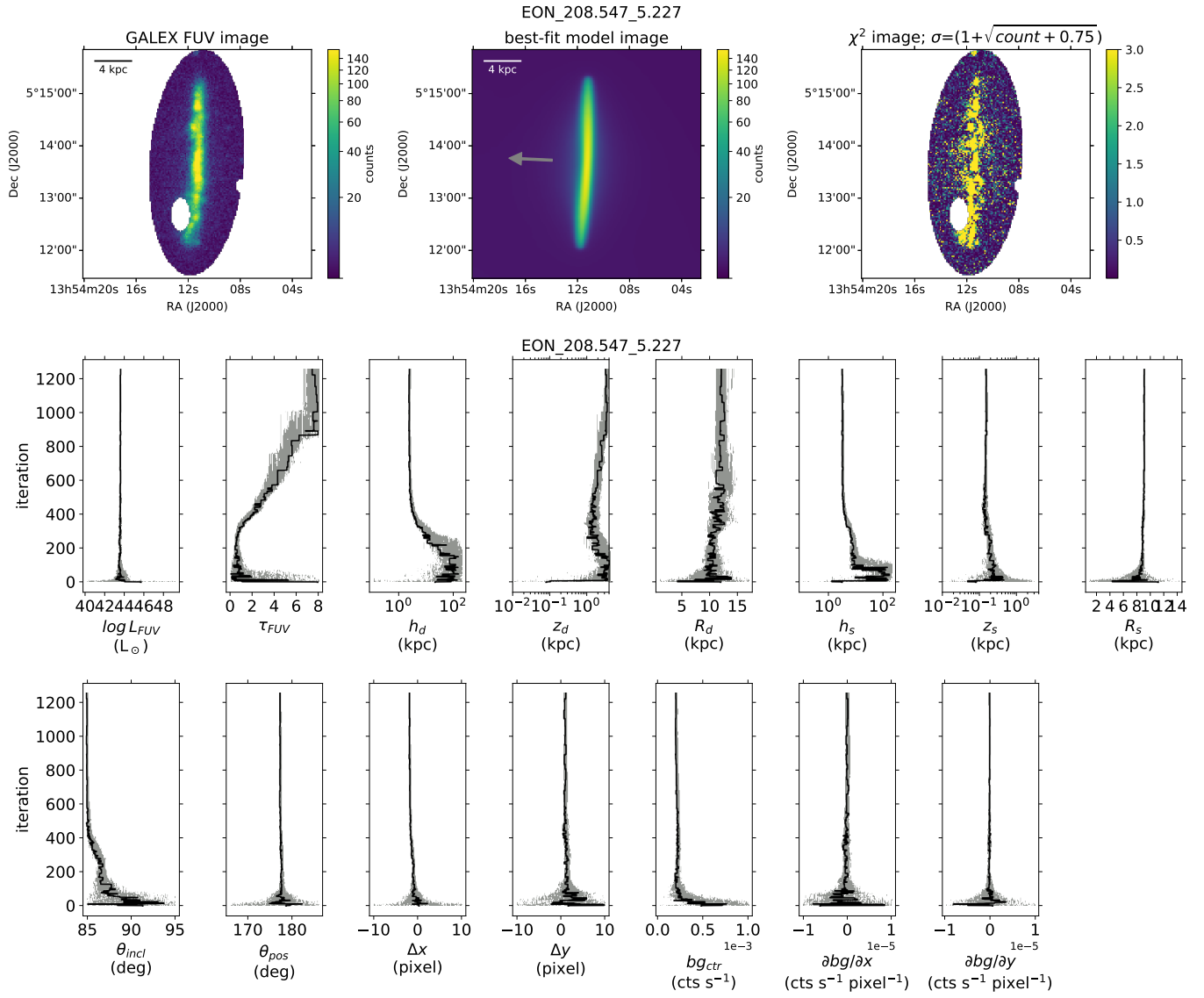


Figure 21. Fitting results for EON_208.547_5.227. The rest are the same as in Fig. 5

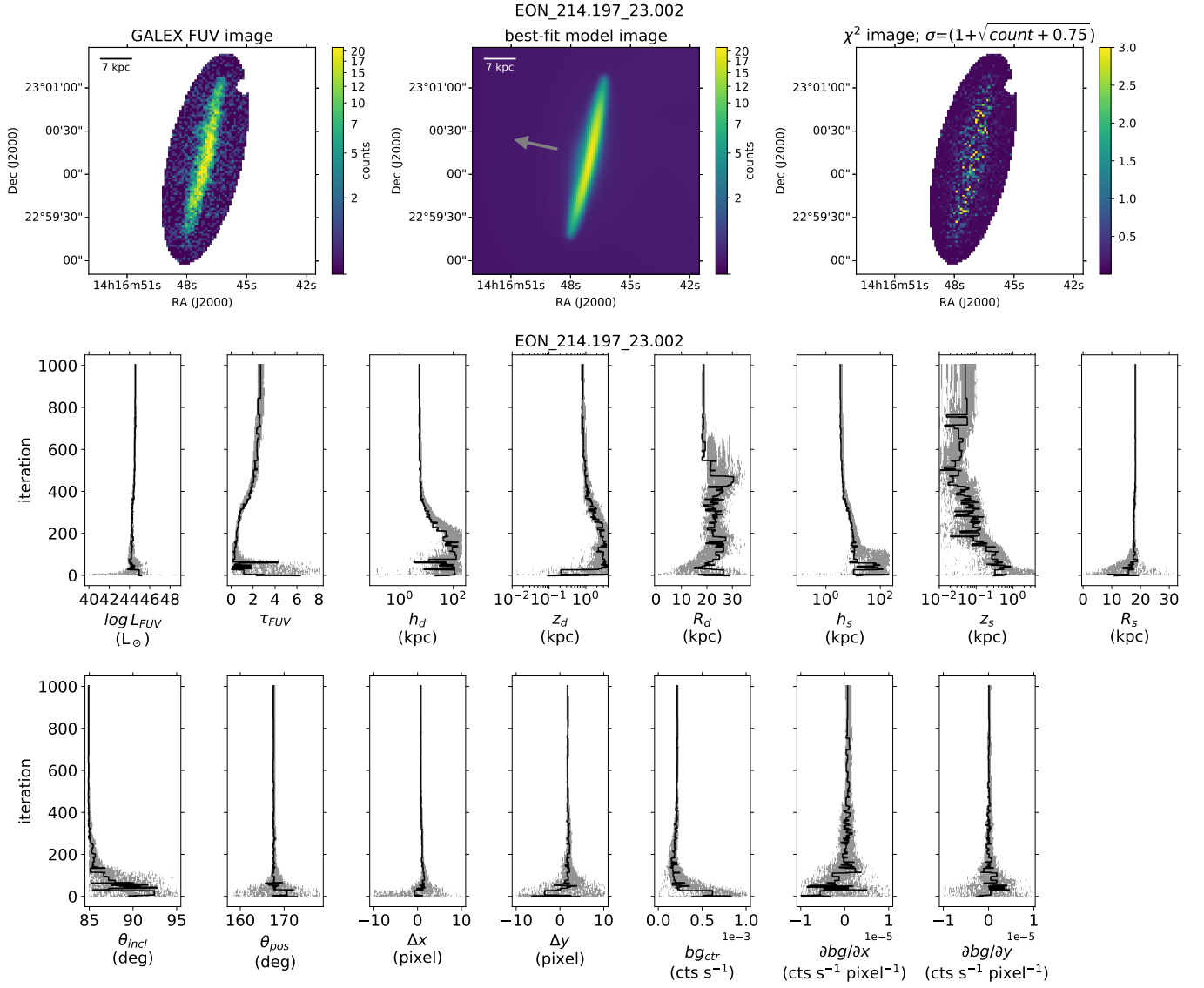


Figure 22. Fitting results for EON_214.197_23.002. The rest are the same as in Fig. 5

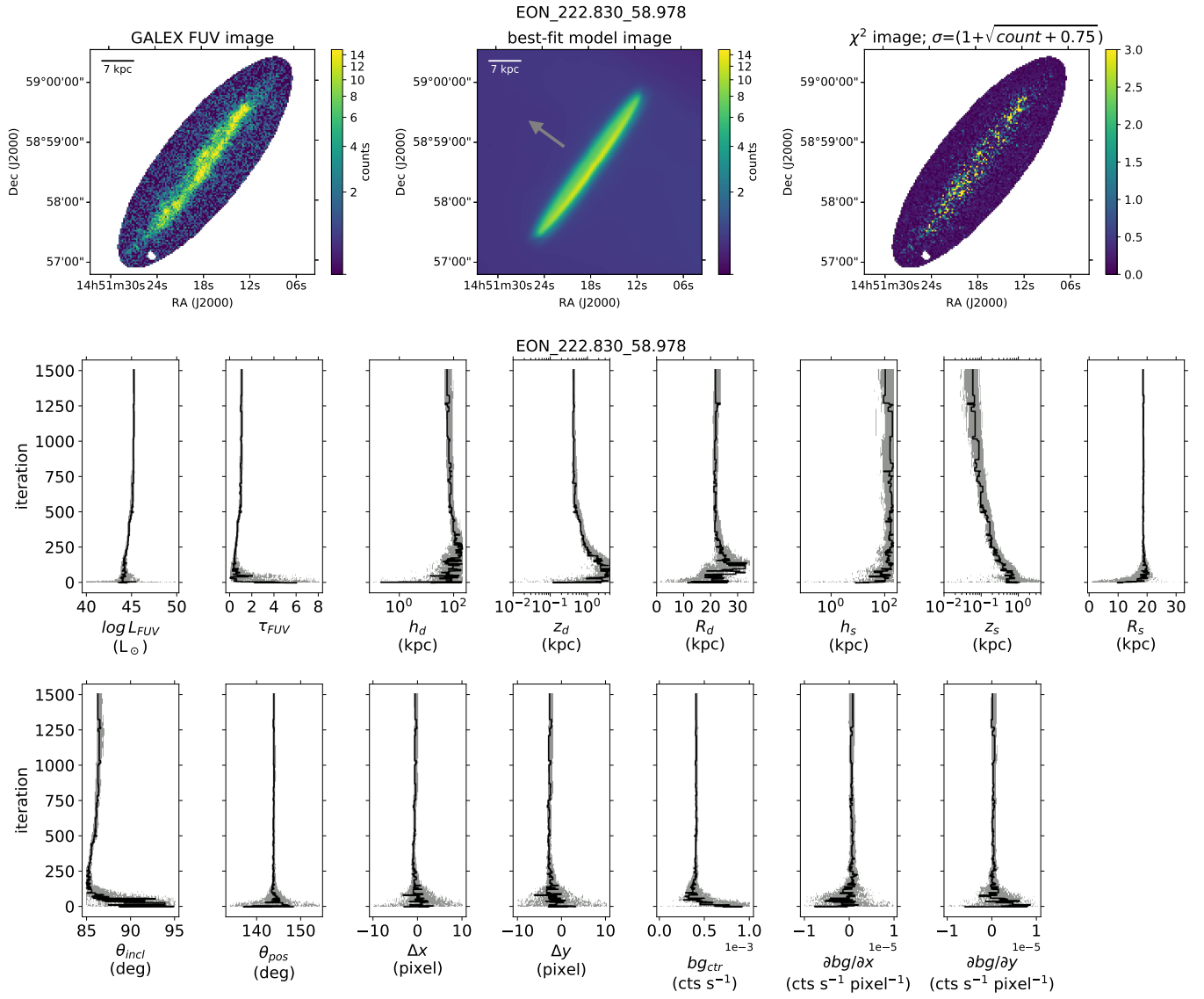


Figure 23. Fitting results for EON_222.830_58.978. The rest are the same as in Fig. 5

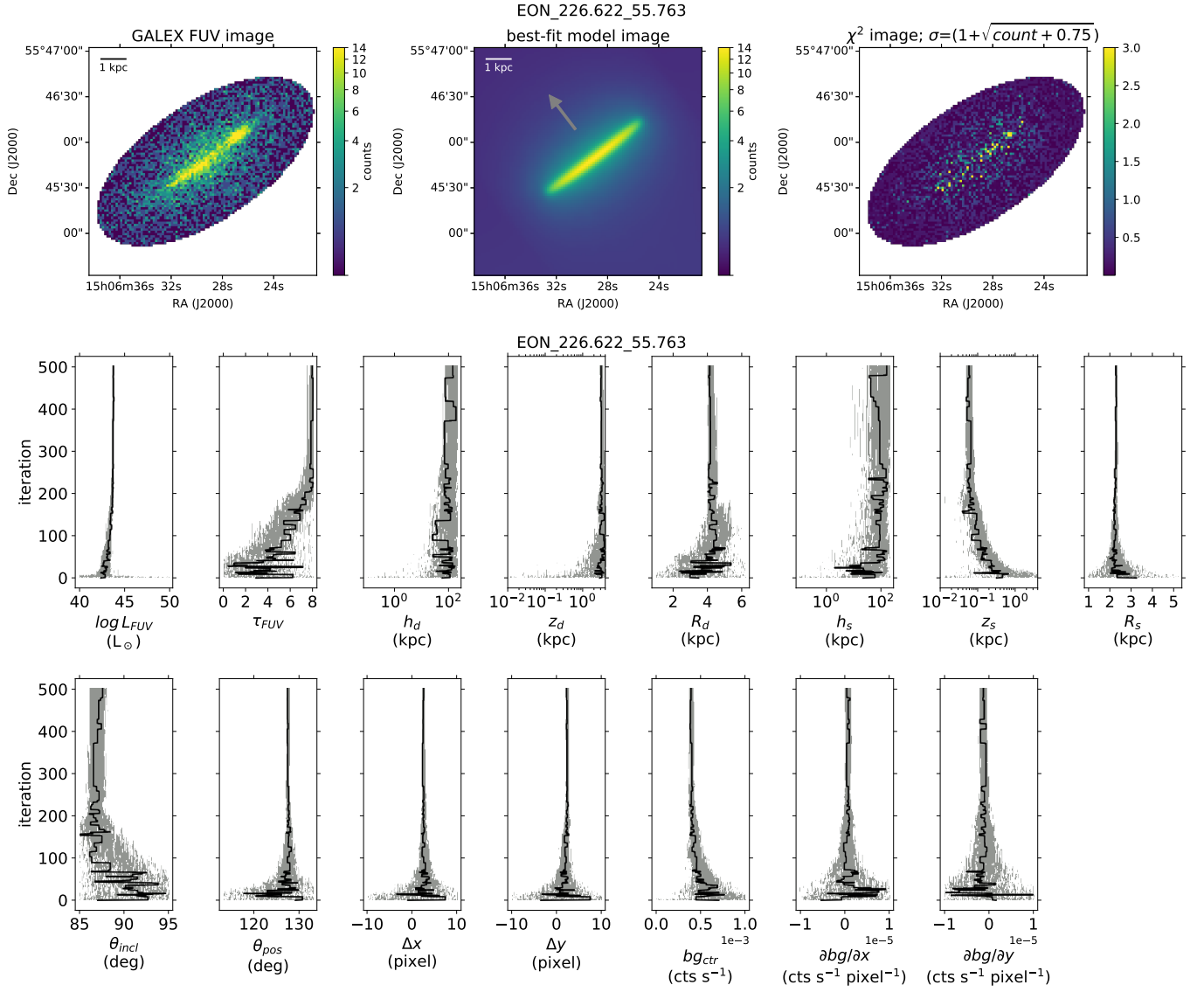


Figure 24. Fitting results for EON_226.622_55.763. The rest are the same as in Fig. 5

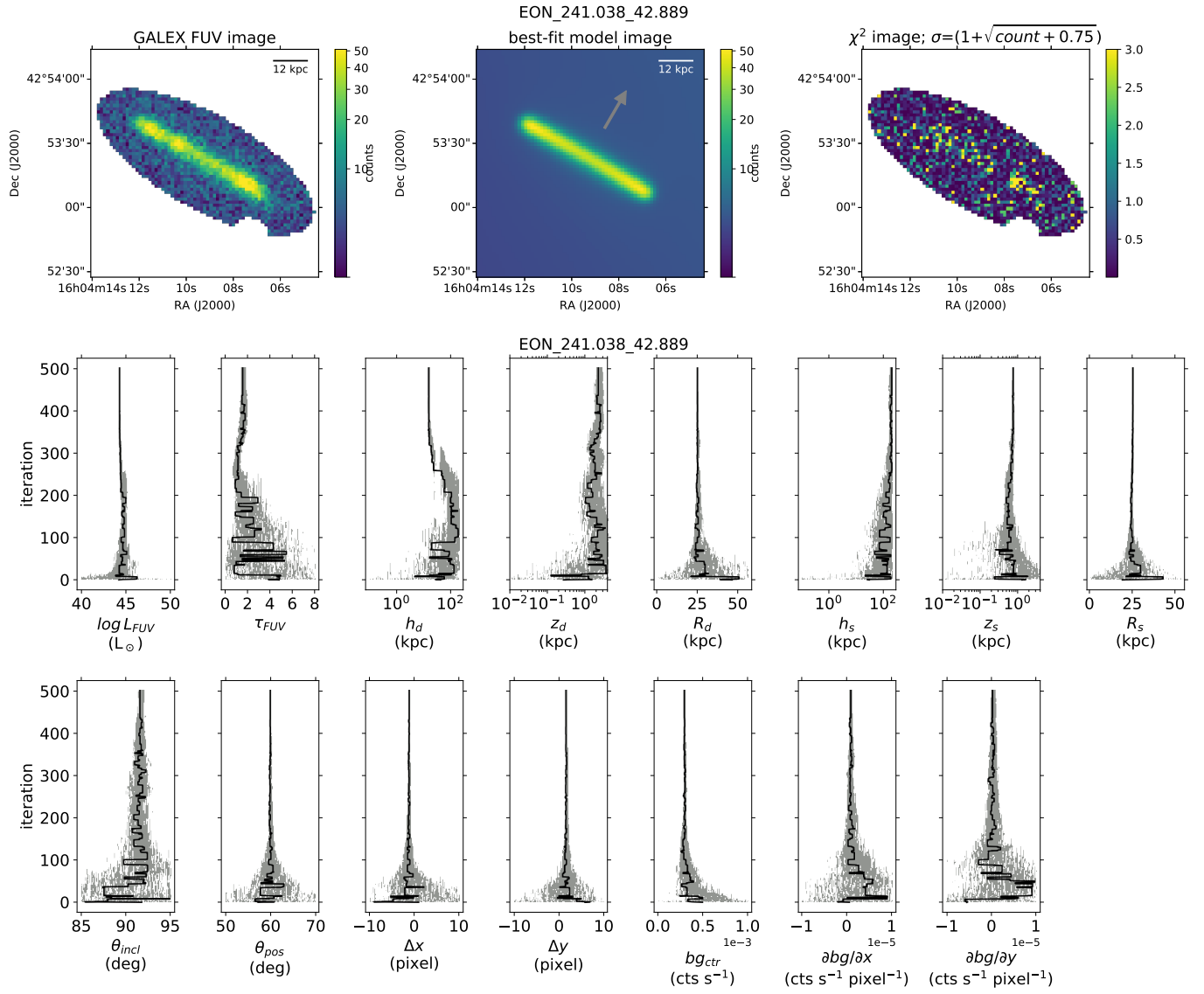


Figure 25. Fitting results for EON_241.038_42.889. The rest are the same as in Fig. 5

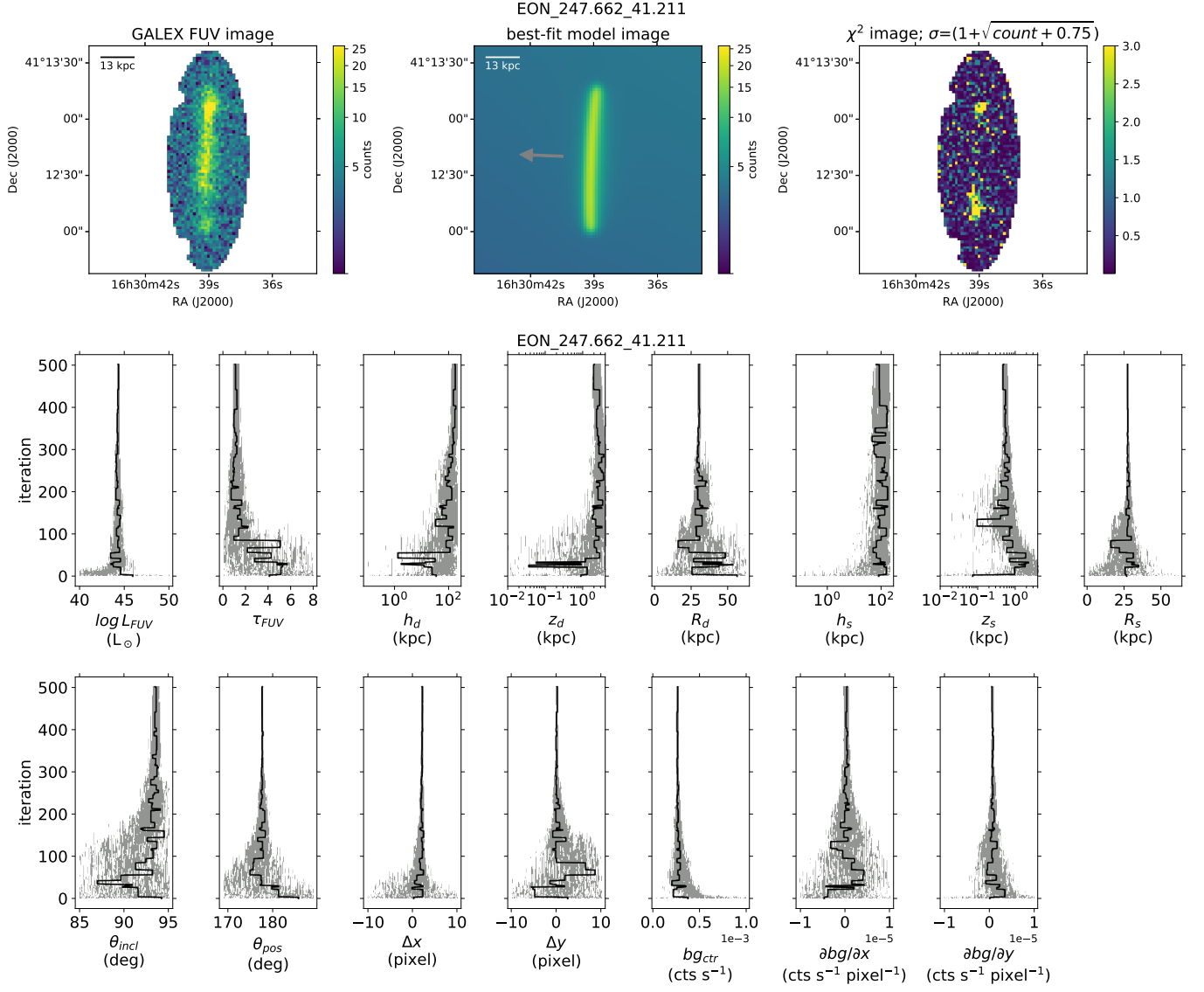


Figure 26. Fitting results for EON_247.662_41.211. The rest are the same as in Fig. 5

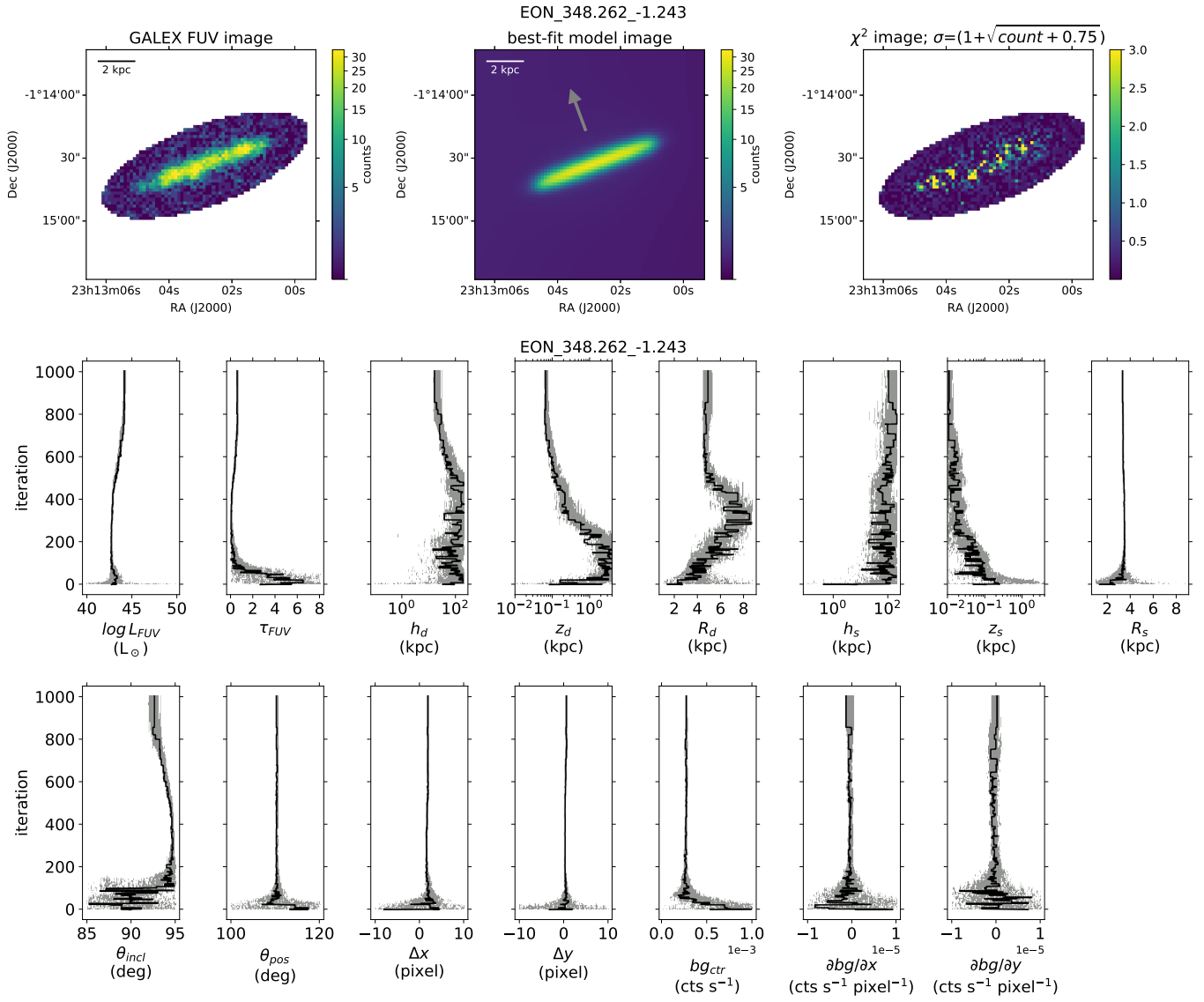


Figure 27. Fitting results for EON_348.262_-1.243. The rest are the same as in Fig. 5

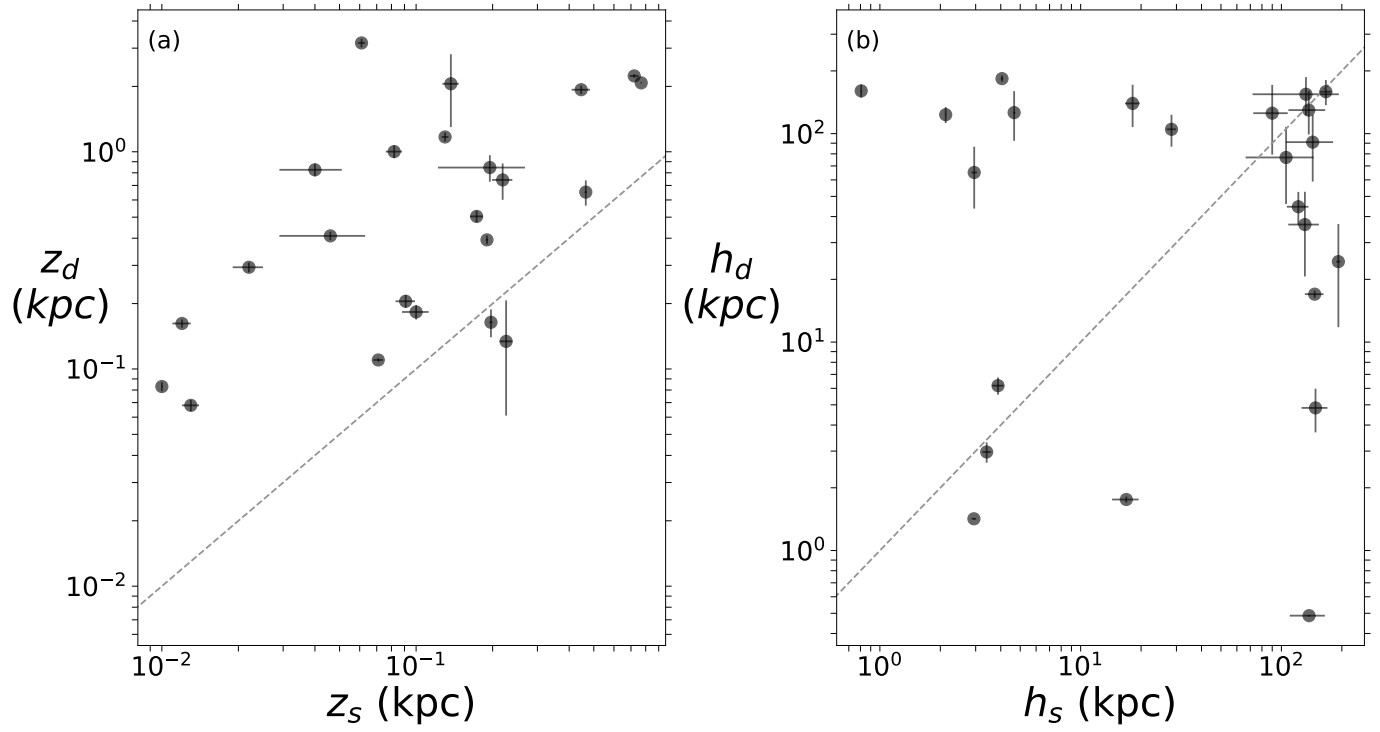


Figure 28. Plots of scale-heights and scale-lengths. (a) light source scale-height vs dust scale-height. (b) light source scale-length vs dust scale-length. The *grey dashed lines* indicate the one-to-one lines.

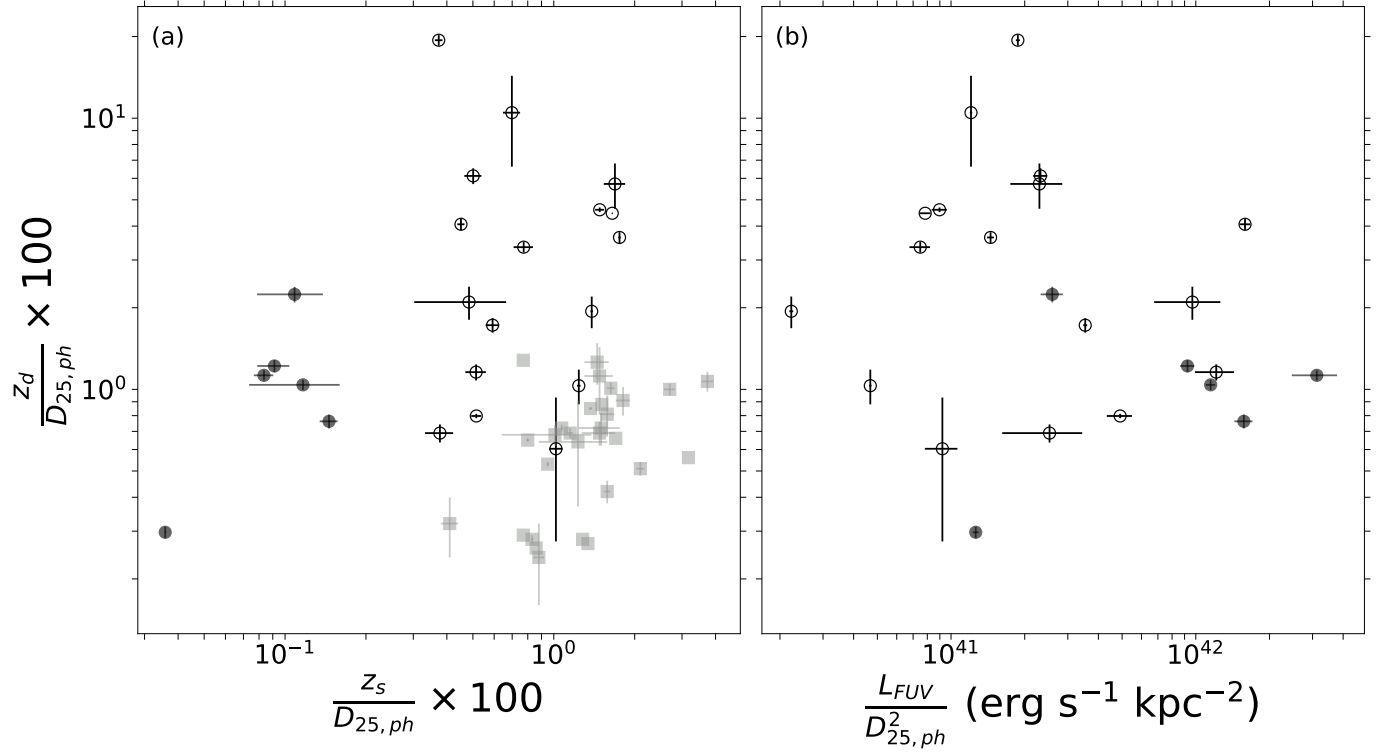


Figure 29. Plots for galaxy-size independent comparisons. (a) the plot between the ratios of scale-height to galactic diameter for light source and dust. *Open* and *filled circles* indicate “high-group” and “low-group,” respectively (see text). *Gray squares* indicate the values obtained from the optical radiative transfer studies of other galaxies (Table 4). (b) the plot between the ratio of dust scale-height to galactic diameter and L_{FUV}/D_{25}^2 which is proportional to the surface density of FUV luminosity. The symbols are the same as in the panel (a).

Table 1. Target Edge-on Galaxies with Relevant Information

ID	Other Name	D_{25}	d	$D_{25,ph}$	Exposure Time	Tile Name
		($''$)	(Mpc)	(kpc)	(s)	
(1)	(2)	(3)	(4)	(5)	(6)	(7)
EON_10.477_41.954	FGC 0079	60	160	46.5	7418	PS_M31_MOS07
EON_12.715_0.851	FGC 0096	70	71	24.1	3223	MISWZS01_29059_0266
EON_17.154_1.641	UGC 00711	228	24	26.5	1682	MISWZS01_30937_0266
EON_20.349_-1.863	FGC 0155	80	41	15.9	3262	MISWZS01_17362_0269
EON_24.788_-10.504	MCG -02-05-030	80	72	27.9	3268	GI1_013020_IRASF0136
EON_123.495_45.742	IC 2233	281	13	17.7	3207	NGA_NGC2537
EON_163.623_17.344	NGC 3454	125	27	16.4	1600	GI2_121006_LGG225_PO
EON_168.614_17.260	NGC 3592	107	25	13.0	3715	GI3_103009_Abell1204
EON_183.320_43.699	NGC 4183	335	18	29.2	1676	GI1_047063_UGC07271
EON_184.175_46.079	UGC 07301	129	23	14.4	13756	PS_NGC4258_MOS26
EON_184.392_22.540	UGC 07321	330	18	28.8	1683	GI4_095024_UGC07321
EON_185.427_14.598	NGC 4302	330	21	33.6	21177	GI2_017001_J121754p1
EON_187.066_9.436	NGC 4445	158	18	13.8	4383	GI5_057003_NGC4445
EON_189.100_40.005	UGC 07774	218	21	22.2	1664	GI4_095042_UGC7774
EON_189.587_7.891	UGC 07802	97	23	10.8	1661	GI2_125005_AGESstrip
EON_197.704_49.893	UGC 08257	66	126	40.3	6255	WDST_J1308p4930
EON_208.547_5.227	NGC 5348	213	19	19.6	16943	PS_VISTA_MOS04
EON_214.197_23.002	UGC 09138	117	65	36.9	1974	GI4_016007_DDO187
EON_222.830_58.978	NGC 5777	185	44	39.5	2488	MISDR1_10146_0610
EON_226.622_55.763	NGC 5866	281	12	16.3	1526	NGA_NGC5866
EON_241.038_42.889	UGC 10171	66	152	48.6	19658	HRC_CLJ1604p4321
EON_247.662_41.211	UGC 10432	81	147	57.7	12687	ELAISN2_01
EON_348.262_-1.243	FGC 2468	80	23	8.9	3152	MISDR1_29149_0381

NOTE—Columns: (1) ID from the edge-on galaxy catalog of Bizyaev et al. (2014), (2) target’s other name, (3) major-axis diameter, (4) distance to the target, (5) D_{25} converted to the physical size using the distance d , (6) *GALEX* FUV exposure time, and (7) *GALEX* exposure tile name. Columns (3)-(4) are from the NASA/IPAC Extragalactic Database (<https://ned.ipac.caltech.edu/>).

Table 2. Best Model Parameters

ID	$\log(L_{FUV}/L_{\odot})$	τ_{FUV}	h_d (kpc)	z_d (kpc)	R_d (kpc)	h_s (kpc)	z_s (kpc)	R_s (kpc)	i ($^{\circ}$)
(1)	(2)	(3)	(4)	(5)	(6)	(7)	(8)	(9)	(10)
EON_10.477_41.954	44.230±0.022	0.990±0.049	104.903±18.309	2.076±0.003	21.890±0.170	28.347±1.466	0.768±0.003	21.600±0.036	85.907±0.182
EON_12.715_0.851	44.730±0.029	0.300±0.022	76.877±30.903	0.294±0.015	14.400±0.285	105.503±39.169	0.022±0.003	9.150±0.078	89.857±0.119
EON_17.154_1.641	44.250±0.156	0.217±0.034	183.633±6.298	0.183±0.014	14.610±0.422	4.057±0.054	0.100±0.012	14.283±0.090	88.457±0.125
EON_20.349_-1.863 ^a	43.073±0.005	5.660±0.150	0.487±0.005	0.164±0.024	13.860±2.080	137.353±27.286	0.197±0.003	6.217±0.005	88.093±0.141
EON_24.788_-10.504 ^a	43.993±0.012	7.960±0.016	1.420±0.008	0.083±0.004	17.777±1.392	2.940±0.075	0.010±0.000	13.407±0.012	93.583±0.045
EON_123.495_45.742	44.580±0.079	0.533±0.059	91.040±32.152	0.205±0.014	9.843±0.226	143.187±37.819	0.091±0.008	8.537±0.024	89.407±0.090
EON_163.623_17.344	43.793±0.029	1.660±0.170	4.833±1.144	1.002±0.067	8.280±0.311	147.863±21.804	0.082±0.006	5.613±0.009	86.820±0.126
EON_168.614_17.260	43.587±0.104	0.323±0.033	123.300±10.831	0.742±0.141	18.780±4.370	2.127±0.005	0.219±0.020	6.330±0.024	86.153±0.774
EON_183.320_43.699	44.480±0.008	0.413±0.009	139.617±32.116	0.504±0.031	22.993±1.827	18.147±1.519	0.173±0.010	11.940±0.062	85.527±0.021
EON_184.175_46.079	44.810±0.091	0.143±0.034	154.507±32.109	0.162±0.007	17.983±3.164	132.530±60.717	0.012±0.001	5.317±0.060	89.997±0.005
EON_184.392_22.540	45.120±0.022	7.940±0.037	158.907±21.919	1.170±0.055	14.220±0.157	166.520±11.402	0.130±0.004	13.953±0.117	91.060±0.028
EON_185.427_14.598	43.400±0.008	7.840±0.102	1.757±0.059	0.652±0.087	16.427±0.154	16.883±2.552	0.465±0.005	13.223±0.097	89.960±0.043
EON_187.066_9.436	43.970±0.051	1.603±0.099	160.400±11.501	0.110±0.002	4.427±0.005	0.807±0.005	0.071±0.003	3.597±0.005	87.003±0.103
EON_189.100_40.005	43.657±0.066	0.177±0.037	126.160±33.766	0.134±0.073	12.383±0.026	4.663±0.065	0.226±0.013	10.857±0.026	85.027±0.031
EON_189.587_7.891	43.230±0.014	0.250±0.014	65.120±21.432	0.393±0.018	5.003±0.026	2.950±0.094	0.190±0.002	4.993±0.012	85.323±0.012
EON_197.704_49.893	45.197±0.131	1.837±0.098	16.977±0.682	0.846±0.118	35.133±0.878	146.487±15.682	0.195±0.073	20.043±0.040	86.470±0.191
EON_208.547_5.227	43.667±0.005	4.263±2.221	2.970±0.332	2.056±0.756	12.877±0.524	3.403±0.163	0.137±0.010	9.003±0.034	85.070±0.045
EON_214.197_23.002	44.547±0.045	2.273±0.304	6.180±0.587	0.826±0.055	17.733±0.662	3.877±0.256	0.040±0.011	17.563±0.429	85.007±0.005
EON_222.830_58.978	45.253±0.019	1.113±0.077	44.593±7.967	0.410±0.018	21.847±0.152	121.420±14.962	0.046±0.017	18.507±0.068	86.487±0.095
EON_226.622_55.763	43.700±0.008	7.910±0.022	129.710±30.591	3.170±0.142	4.280±0.167	136.867±28.485	0.061±0.002	2.317±0.005	87.280±0.361
EON_241.038_42.889	44.327±0.031	1.470±0.259	24.327±12.541	2.235±0.044	25.287±0.135	192.220±4.596	0.721±0.028	25.283±0.139	91.693±0.120
EON_247.662_41.211	44.397±0.042	1.140±0.073	125.353±46.002	1.931±0.086	30.410±0.792	89.987±17.540	0.446±0.037	27.917±0.316	93.260±0.166
EON_348.262_-1.243	44.097±0.037	0.603±0.025	36.630±15.969	0.068±0.004	4.810±0.177	130.910±22.734	0.013±0.001	3.373±0.024	92.970±0.227

NOTE—Model parameters for the viewpoint and the background, except the inclination, are excluded for simplicity. The errors are set as the standard deviation of the best-fit parameters obtained from three independent fitting runs, in a similar way to De Geyter et al. (2013) and De Geyter et al. (2014).

^aThe model parameters for these targets should be handled with cautions. The two prominent clumps of emission, seen along the galactic disk at the symmetric positions, might be real emitting clumps rather than the effect of radiative transfer.

Table 3. Ratio of Scale-height to Galactic Diameter

ID	$\frac{z_s}{D_{25,ph}} \times 100$	$\frac{z_d}{D_{25,ph}} \times 100$	symbol ^a
(1)	(2)	(3)	
EON_10.477_41.954	1.650±0.006	4.461±0.006	○
EON_12.715_0.851	0.091±0.012	1.220±0.062	●
EON_17.154_1.641	0.377±0.045	0.690±0.053	○
EON_20.349_-1.863 ^b	1.239±0.019	1.031±0.151	○
EON_24.788_-10.504 ^b	0.036±0.000	0.297±0.014	●
EON_123.495_45.742	0.514±0.045	1.158±0.079	○
EON_163.623_17.344	0.501±0.037	6.125±0.410	○
EON_168.614_17.260	1.689±0.154	5.721±1.087	○
EON_183.320_43.699	0.592±0.034	1.724±0.106	○
EON_184.175_46.079	0.083±0.007	1.127±0.049	●
EON_184.392_22.540	0.451±0.014	4.062±0.191	○
EON_185.427_14.598	1.384±0.015	1.940±0.259	○
EON_187.066_9.436	0.515±0.022	0.798±0.015	○
EON_189.100_40.005	1.018±0.059	0.604±0.329	○
EON_189.587_7.891	1.756±0.018	3.632±0.166	○
EON_197.704_49.893	0.484±0.181	2.098±0.293	○
EON_208.547_5.227	0.698±0.051	10.479±3.853	○
EON_214.197_23.002	0.108±0.030	2.240±0.149	●
EON_222.830_58.978	0.117±0.043	1.039±0.046	●
EON_226.622_55.763	0.373±0.012	19.388±0.869	○
EON_241.038_42.889	1.482±0.058	4.595±0.090	○
EON_247.662_41.211	0.773±0.064	3.345±0.149	○
EON_348.262_-1.243	0.146±0.011	0.762±0.045	●

^aThe corresponding symbol in Fig. 29. ● is “low-group”, while ○ is “high-group.”

^bThese targets should be handled with cautions since there are some ambiguity in the best-fit model parameters. See Table 2.

Table 4. Ratio of Scale-height to Galactic Diameter from Optical Radiative Transfer Studies

Name	$\frac{z_s}{D_{25,ph}} \times 100$	$\frac{z_d}{D_{25,ph}} \times 100$	z_s	z_d	$D_{25,ph}$	D_{25}	d	Reference
(1)	(2)	(3)	(kpc)	(kpc)	(kpc)	($''$)	(Mpc)	(9)
IC 2098	1.48±0.21	0.69±0.07	0.430±0.060	0.200±0.020	29.06	125.40	47.80	De Geyter et al. (2014)
IC 2461	0.41±0.03	0.32±0.08	0.150±0.010	0.120±0.030	36.97	140.70	54.20	De Geyter et al. (2014)
IC 2531	0.95±0.01	0.53±0.01	0.422±0.006	0.236±0.006	44.27	415.10	22.00	Xilouris et al. (1999)
IC 3203	1.58±0.04	0.42±0.04	0.830±0.020	0.220±0.020	52.47	90.80	119.20	De Geyter et al. (2014)
IC 4225	3.73±0.18	1.07±0.09	0.840±0.040	0.240±0.020	22.50	62.80	73.90	De Geyter et al. (2014)
NGC 3650	2.10±0.07	0.51±0.03	0.620±0.020	0.150±0.010	29.49	101.90	59.70	De Geyter et al. (2014)
NGC 3987	2.70±0.13	1.00±0.05	1.080±0.050	0.400±0.020	39.98	134.30	61.40	De Geyter et al. (2014)
NGC 4013	1.15±0.03	0.69±0.03	0.203±0.006	0.123±0.006	17.71	314.90	11.60	Xilouris et al. (1999)
NGC 4013	1.01±0.37	0.68±0.06	0.287±0.104	0.192±0.016	28.40	314.90	18.60	De Geyter et al. (2013)
NGC 4013	1.70	0.66	0.376	0.145	22.14	314.90	14.50	Bianchi (2007)
NGC 4175	1.48±0.18	1.12±0.31	0.330±0.040	0.250±0.070	22.34	109.20	42.20	De Geyter et al. (2014)
NGC 4217	0.77	1.28	0.199	0.331	25.80	314.90	16.90	Bianchi (2007)
NGC 4302	3.17	0.56	1.023	0.181	32.29	329.70	20.20	Bianchi (2007)
NGC 4565	0.86	0.26	0.672	0.205	77.91	950.90	16.90	de Looze et al. (2012)
NGC 5166	1.58±0.10	0.81±0.14	0.660±0.040	0.340±0.060	41.73	137.50	62.60	De Geyter et al. (2014)
NGC 5529	0.80±0.01	0.65±0.01	0.425±0.007	0.345±0.007	53.10	370.00	29.60	Xilouris et al. (1999)
NGC 5529	0.77	0.29	0.581	0.218	75.16	370.00	41.90	Bianchi (2007)
NGC 5746	1.51	0.88	0.865	0.505	57.36	444.80	26.60	Bianchi (2007)
NGC 5907	0.83±0.01	0.28±0.01	0.333±0.006	0.113±0.006	40.29	755.40	11.00	Xilouris et al. (1999)
NGC 5908	0.88±0.04	0.24±0.08	0.440±0.020	0.120±0.040	50.28	194.20	53.40	De Geyter et al. (2014)
NGC 5965	1.34	0.27	0.969	0.194	72.36	314.90	47.40	Bianchi (2007)
NGC 891	1.07±0.01	0.72±0.02	0.400±0.004	0.267±0.006	37.28	809.40	9.50	Xilouris et al. (1999)
NGC 891	1.23±0.35	0.64±0.27	0.460±0.130	0.240±0.100	37.28	809.40	9.50	Schechtman-Rook et al. (2012)
UGC 1082	1.63±0.05	1.01±0.05	0.452±0.013	0.278±0.013	27.66	154.20	37.00	Xilouris et al. (1999)
UGC 12518	1.50±0.26	0.72±0.10	0.290±0.050	0.140±0.020	19.34	77.30	51.60	De Geyter et al. (2014)
UGC 2048	1.37±0.02	0.85±0.01	0.933±0.012	0.577±0.006	68.08	222.90	63.00	Xilouris et al. (1997)
UGC 4136	1.81±0.11	0.91±0.11	0.660±0.040	0.330±0.040	36.45	82.80	90.80	De Geyter et al. (2014)
UGC 4277	1.28	0.28	1.104	0.245	86.56	233.40	76.50	Bianchi (2007)
UGC 5481	1.45±0.15	1.26±0.22	0.590±0.060	0.510±0.090	40.63	92.90	90.20	De Geyter et al. (2014)

NOTE—Columns: (1) galaxy name, (2) ratio for light source, (3) ratio for dust, (4) light source scale-height, (5) dust scale-height, (6) major-axis diameter in kpc, (7) major-axis diameter in arcsec which is obtained from the NASA/IPAC Extragalactic Database (<https://ned.ipac.caltech.edu/>), (8) distance to the galaxy, and (9) the reference which provides z_s , z_d , and d . Columns (2)-(3) are calculated from Columns (4)-(6). For Columns (4)-(5), we quote a weight-averaged mean and its error when multiple estimations are available. Column (6) is calculated from Columns (7)-(8).